User's Guide for the Limb Radiance Inversion Radiometer (LRIR) Data Set

John C. Gille
Paul L. Bailey
Gail P. Anderson
Sharon A. Beck
Cheryl A. Craig
William J. Kohri
Stanley C. Nolte
Verrill J. Rinehart

National Center for Atmospheric Research
Boulder, Colorado 80307

February 1984

Preface

The Nimbus 6 Limb Radiance Inversion Radiometer (LRIR) was the first infrared limb scanner to fly on a satellite. As might have been expected with a new measurement approach, development of the instrumentation required the solution of a number of challenging problems. Similarly, the reduction of this new type of data required the development of many new techniques and diagnostic capabilities. The final responsiblity came down to a rather small group at NCAR, which worked several years to reduce and refine the data to their present state.

These data provide temperature and ozone profiles with high vertical resolution from $\sim$ 15 km to $\sim$ 64 km, between 14 June 1975 and 7 January 1976, when the solid cryogen used to cool the detectors was depleted. As such, they contain unique information about the middle atmosphere.

This User's Guide has been prepared to assist others to understand and use the LRIR data. We would appreciate feedback about the data and this guide from those who use them.

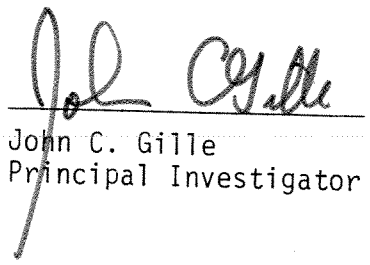

John C. Gille
Principal Investigator

CONTENTS

Section 1

INTRODUCTION

The Limb Radiance Inversion Radiometer (LRIR), initially known as the Limb Radiance Inversion Experiment, was first proposed in November 1968, in response to the NASA Announcement of Flight Opportunity for Nimbus F. Dr. John C. Gille, then of Florida State University, was the Principal Investigator, with the late Prof. Richard A. Craig of Florida State University and Prof. Frederick B. House, then of GCA Corporation, as Co-Investigators, with Honeywell Corporation as the instrument contractor. Subsequently Gille moved to the National Center for Atmospheric Research (NCAR), and House to Drexel University. After the initial evaluation, a phase A study was carried out during 1970 which demonstrated the feasibility of obtaining high quality atmospheric results using available radiometric technology, without the necessity for very high accuracy attitude and tracking data. Following final selection, hardware fabrication began in late 1971.

The flight model hardware was delivered at the end of 1974, for integration on the spacecraft. Launch took place on 12 June 1975. The LRIR was first turned on at the beginning of Orbit 35, on 14 June, and operated satisfactorily thereafter.

LRIR was operated at a 50% duty cycle until late October 1975. From then until 7 January 1976 it was operated at about 90% duty cycle. At that time the supply of methane in the solid cryogen cooler was completely expended and further collection of useful data ceased.

Following launch, the science and data reduction team worked to put the raw data into manageable form, convert them into radiance profiles,

invert those profiles, and demonstrate that limb scanning is a powerful and feasible method for observing the stratosphere and mesosphere.

The resulting data, in the form of profiles of temperature and ozone every 4° of latitude, from approximately 100 mb (15 km) to 0.1 mb (64 km) have now been archived at the National Space Science Data Center (NSSDC). This User's Guide provides information on the experiment and the data to assist others in using the data. Section 2 repeats the experiment description from the pre-launch Nimbus 6 User's Guide, and presents additional information on orbital performance. The processing of LRIR data is described in Section 3, and the evaluation of data quality is presented in Section 4. Data coverage is outlined in Section 5, and details of the tape specifications are given in Section 6. The Appendix contains a bibliography of papers related to LRIR data, as well as two reprints discussing the validation of the data and outlining some data applications.

Section 2

EXPERIMENT DESCRIPTION

Section 2.1 is reproduced from Section 7 of the Nimbus 6 User's Guide which was written before launch, and before all test results were available. Sections 2.2-2.9 are post-launch updates.

PRE-LAUNCH EXPERIMENT DESCRIPTION, FROM THE NIMBUS 6 USER'S GUIDE

SECTION 7

THE LIMB RADIANCE INVERSION RADIOMETER (LRIR) EXPERIMENT

by

J. C. Gille* and P. Bailey, NCAR, Boulder, Colorado 80303
F. B. House, Drexel University, Philadelphia, Pennsylvania 19104
R. A. Craig, Florida State University, Tallahassee, Florida 32301
J. R. Thomas, Honeywell Radiation Center, Lexington, Mass. 02173

7.1 Introduction

The Limb Radiance Inversion Radiometer (LRIR) experiment is being conducted to determine the vertical distribution of temperature, ozone, and water vapor from the lower stratosphere (~15 km) through the stratosphere and into the lower mesosphere (~60 km) on a global scale. These vertical distributions will be determined by inverting measured limb radiance profiles obtained by the LRIR, an infrared, multispectral scanning radiometer aboard the Nimbus 6 spacecraft. Measurements are made in each of four spectral regions: two in the 15 μm carbon dioxide band; one in the 9.6 μm ozone band; and one located in the rotational water vapor band (23 μm to 27 μm).

A programmed scanning mirror in the radiometer causes the fields-of-view of the four detectors to make coincident, vertical scans across the earth's horizon. (See Figure 7-1 for description of limb-viewing geometry.) The data from these scans are stored on a HDRSS tape recorder for later transmission to the ground. During data reduction the measured limb radiance profiles from the carbon dioxide channels are operated on by inversion algorithms to determine the vertical temperature distribution. This inferred temperature profile, together with the radiance profiles in the ozone and water vapor channels, are then used to infer the vertical distribution of these trace constituents.

Spacecraft hardware consists of a frame housing assembly (FHA) and two electronics units: the frame housing electronics unit (FEU) and the interface electronics unit (IEU). The FHA consists of an optical mechanical package (OMP) and a two-stage solid ammonia-methane cryogen package (SCP) for detector cooling. The FEU conditions radiance signals, controls the scan drive mechanism,

*John C. Gille is principal investigator of the LRIR experiment and coordinates activities of the Science Team, composed of the members above.

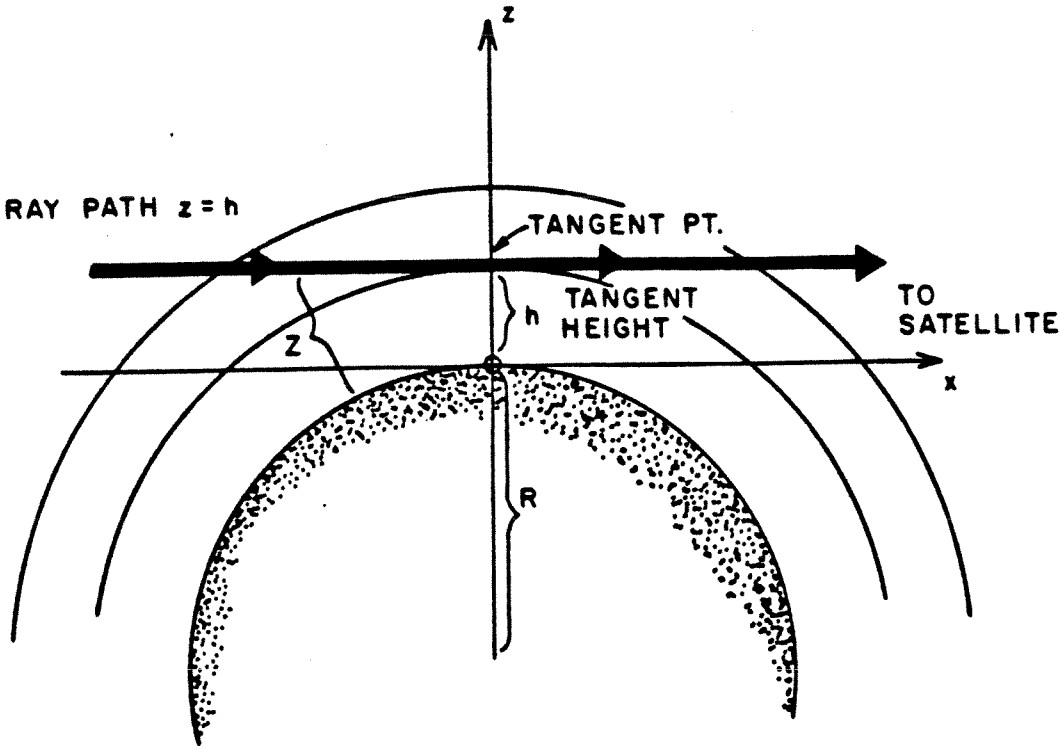

Figure 7-1. LRIR Limb Viewing Geometry

and contains the command relay and command logic assemblies. The IEU interacts with spacecraft systems and performs the functions of signal processing, control, power conversion and digitizing of electronic signals.

7.2 Experiment Concept

The scientific objectives of the LRIR experiment are to:

- Acquire and present global measurements of temperature, ozone and water vapor in the stratosphere and lower mesosphere for one year
- Obtain the geostrophic component of the wind up to a level of 1 mb (~48 km) through integration of the temperature profile in the thermal wind equation

In order to meet these scientific objectives, specifications were placed on the instrument design to provide observations of sufficient quality to yield atmospheric parameters to the desired accuracy and precision. In this regard, minimum scientific data requirements were established as indicated in Table 7-1. Instrument specifications were determined relative to these data requirements.

Table 7-1
LRIR Science Data Requirements

Parameter	Accuracy	Vertical Resolution of Parameters	Altitude Range
Temperature	±3°K RMS	3 km	15-54 km
Ozone	±20% at 1 mb	3 km	15-48 km (1 mb)
Water Vapor	±50% at 1 mb	3 km below 30 km 4-5 km above 30 km	15-48 km (1 mb)
Geostrophic winds	±10 m/sec (Thickness ±70 m or $\bar{T}$ to ±1.5°K)	Winds at 5, 2 and 1 mb	to 48 km (1 mb)

Referring to Figure 7-1, LRIR receives infrared radiation emitted by the atmosphere along a ray path that may be identified by the height (tangent height) or point (tangent point) closest to the surface. The atmosphere may be scanned by sweeping the view direction from tangent heights < 0 (ray paths intersecting the surface) to large positive values. The following advantageous features of limb scanning are apparent from a consideration of Figure 7-1.

- High inherent vertical resolution

  For geometric reasons, a small portion of the signal originates from below the tangent height, and most of the signal originates from a 4 km to 5 km layer above the tangent height.

- Zero background

  For $h > 0$, all radiation received originates in the atmosphere, and all variations in signal are due to the atmosphere since the radiation is viewed against the cold background of space.

- Large opacity

  There is at least 60 times more emitting gas along a horizontal path grazing the surface than there is in a vertical path to the tangent point. Thus, the atmosphere can be sampled to high altitudes.

There are, of course, disadvantages associated with these features. The long paths mean that even for rather transparent spectral regions, it will be difficult to see the solid surface of the planet. A cloud along a path will act as

a body of infinite opacity, and may cause a considerable alteration in the emerging radiation. For the earth's atmosphere, where clouds are present but usually below the tropopause, these facts suggest that reliable operation will be limited to the upper troposphere and above, with even the coverage of the upper troposphere and lower stratosphere being subject to occasional interruption. For these reasons parameters are determined only above a nominal tropopause at 15 km.

The radiative transfer equation for a non-scattering atmosphere in local thermodynamic equilibrium may be written as

$$I_i(h) = \int_{-\infty}^{\infty} B_i[T] \frac{d\tau_i(h;x)}{dx} dx \,, \qquad (1)$$

where I is the observed radiance at tangent height h and spectral interval i, B is the Planck blackbody function, T is temperature, x the distance coordinate along the ray path, with the origin at the tangent point and positive toward the satellite (located at $+\infty$), and $\tau(h; z)$ the mean transmission in the spectral interval along the path with tangent height h from point x to the satellite.

The temperature inversion problem is to determine B and therefore T from measurements of I, assuming that $d\tau/dx$ is known. The latter requires that the distribution of the emitting species be known, which in practice means that radiation from CO_2, a uniformly mixed gas, is measured. In the limb problem $d\tau/dx$ is also crucially affected by the atmospheric structure.

In the case of the constituent inversion problem, the solution to the temperature inversion problem is utilized with the constituent limb radiance profile to determine the gas concentration as a function of altitude. In Equation (1), B is known from the temperature solution. The constituent concentration is determined as an implicit function of transmission $\tau_i(h; x)$.

In order to gain a better understanding of the data to be observed by the LRIR, examples of calculated profiles of limb radiance as functions of tangent height are shown from a mid-latitude winter sounding in Figure 7-2.

The broad (BCO_2) channel refers to the 585-705 cm^{-1} spectral band, and the narrow (NCO_2) channel covers the band 630-685 cm^{-1}. The signals are quite similar at upper levels where only the strong lines near the centers of the bands are contributing. Below about 30 km, the BCO_2 signal is much larger because the weaker lines in the band wings are contributing energy from the lower atmosphere. The dashed line presents the difference between BCO_2 and NCO_2 signals, or the contribution from the 585-630 cm^{-1} and 685-705 cm^{-1} regions. The

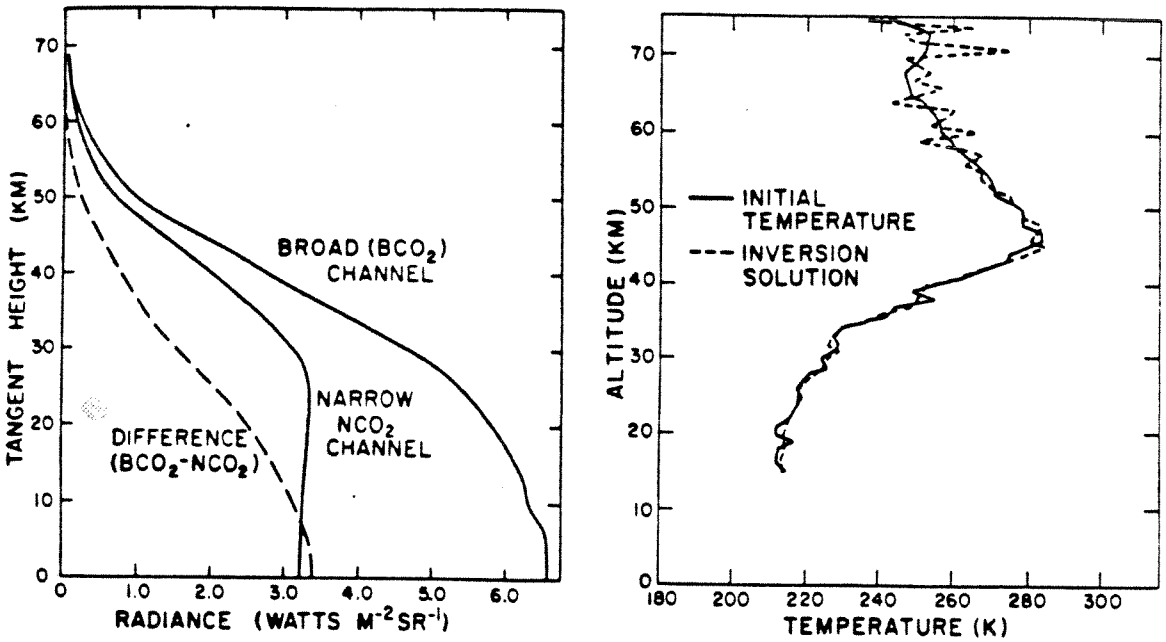

Figure 7-2. Computed Limb Radiances as a Function of Tangent Height for Broad (585-705 cm^{-1}) and Narrow (630-685 cm^{-1}) Channels in the 15 μm Band of CO_2.

steeply sloping portions of the curve occur in situations where the whole path through the atmosphere is moderately transparent, and an appreciable portion of the signal is coming from the tangent point. Figure 7-2 demonstrates that the BCO_2 minus NCO_2 region provides better information on the lower levels of the stratosphere and upper levels of the troposphere.

The profile depicting inversion results in Figure 7-2 illustrates a realistic solution for typical instrument errors, defined by the science requirements in Table 7-1. These results are based on computed limb radiance profiles in Figure 7-2 which were perturbed for realistic radiometer and pointing errors, and included a 1.5 km instrumental field-of-view. The procedures for inverting CO_2 radiance profiles to obtain a solution to the temperature distribution are presented in a paper by Gille and House (Reference 1). The inversion results in Figure 7-2 are in good agreement with the initial temperature profile up to about the 55 km level but become more and more "saw-toothed" in nature at higher altitudes. This characteristic is caused by the random error of the instrument which dominates the natural limb signal at high altitudes. In other words, the signal-to-noise ratio of the measurement becomes increasingly smaller as the LRIR scans to higher altitudes. One obvious procedure to employ in the data processing of real observations is to mathematically smooth the solutions

at higher altitudes and/or average adjacent limb profiles before inversion. Mathematical smoothing techniques can also be employed during the inversion procedure.

Solutions to the constituent inversion problem for vertical distributions of ozone and water vapor show characteristics similar to the temperature of inversion results in Figure 7-2. The saw-toothed character of the solution develops in a similar manner and altitude for ozone distributions, but at about a 40 km level for water vapor distributions, since the signal-to-noise ratio degrades at a lower altitude.

7.3 Instrumentation

In some respects the LRIR instrumentation is similar to nadir viewing experiments, but in other respects it is considerably different. For example, the radiometer employs a fixed array of cooled detectors whose optical views are directed by a scanning mirror. However, the LRIR scan angle is nominally ±1 degree about the earth's horizon, whereas other instruments, like THIR, scan from horizon to horizon across the earth scene. The detectors for LRIR are cooled by a two-stage solid cryogen package incorporating solid ammonia and methane dewars, maintaining the detectors at 65°K. This mechanism of detector cooling is quite different from more widely used radiative coolers.

Since LRIR has a different viewing geometry from nadir viewing experiments, the discussion in this section of the User's Guide first considers the physical location of LRIR on the satellite and the position of view relative to the satellite and relative to the earth's limb. This discussion will help potential users of LRIR data to better understand the relationship between these data and other observations from Nimbus 6. These discussions are followed by details of LRIR instrumentation.

7.3.1 LRIR Location and Limb Viewing Geometry

The information presented in Figure 7-3 illustrates the principal axes of Nimbus 6 and the location of the LRIR relative to these axes and the sensory ring (a). Also shown are associated positions of the optical axis of the radiometer relative to the local horizontal (b) and to the spacecraft heading (c).

As mentioned in Section 7.1, the FHA consists of two components; the cryogen cooler (SCP) and radiometer optics (OMP). The SCP is located to the rear of the sensory ring and directly along the roll axis of the satellite. The OMP is situated beneath the sensory ring with the attached SCP projecting up through

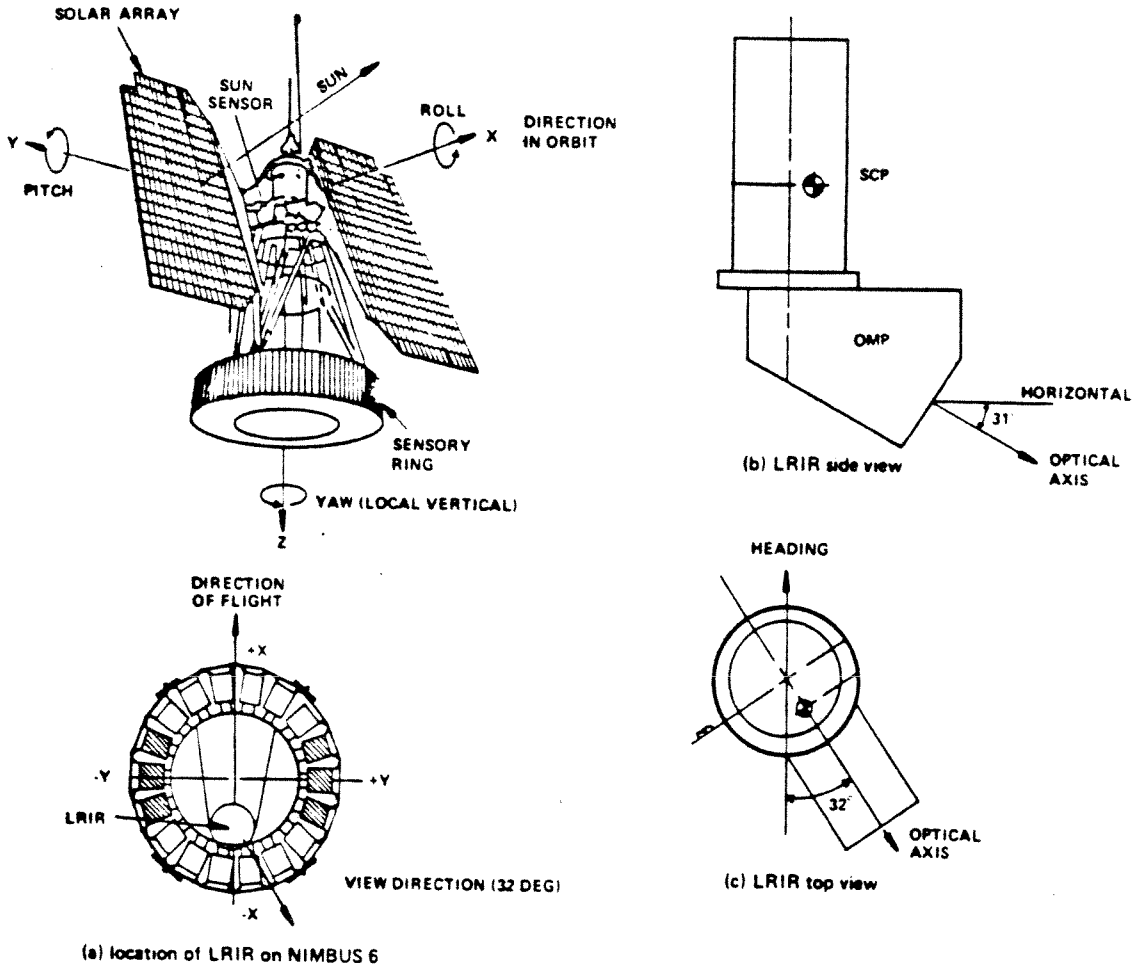

Figure 7-3. Location of the LRIR Instrumentation on the Nimbus 6 Sensory Ring and Associated Viewing Geometry

the ring on the inside. The optical axis of the OMP is positioned 32 degrees to the left of the negative roll axis (-X) in the X-Y plane and 31 degrees below the horizontal of the sensory ring. This positioning is necessary to shield the radiometer from direct solar radiation and to position the mirror scan some 30 to 40 km above the earth's horizon. The mirror in the OMP scans "up and down" through a small angle just above the earth's surface.

It should be emphasized that LRIR views neither the local nadir nor in the orbital plane of the spacecraft. The azimuth of the scan plane is fixed at 32 degrees off the direction of flight. The elevation axis of the scan plane is about 0.6 degrees above the earth's horizon. As a result, the LRIR scan track, when projected to earth, is parallel and to the right of the subpoint track relative to

direction of flight. When the satellite is near the north pole, the LRIR views across the pole. Near the south pole the LRIR views equatorward of the sub-point latitude position. With this geometric configuration, a greater density of observations are provided in the Northern Hemisphere as compared to the Southern Hemisphere. Thus, LRIR data coverage extends from about latitude 83°N to 64°S.

To better understand the LRIR coverage, computer portrayals of successive scan tracks for both hemispheres are presented in Figures 7-4 and 7-5. Note in Figure 7-4 that successive ascending and descending node scans provide equal spacing in mid-latitudes of the Northern Hemisphere in order to provide good spatial coverage in this geographical region of the earth.

7.3.2 Instrument Configuration

The LRIR instrument configuration is shown schematically in Figure 7-6. The limb radiance enters the baffled aperture, reflects off the plane scanning mirror, is focused by the primary parabolic mirror through a field stop and collimator via relay optics to the cooled detectors. Details of the SCP and the functional position of the electronics units are also shown in Figure 7-6. (See Figure 7-8 for more details of electronic units.)

The scan mirror can view the earth's horizon by scanning through a ±5 degree angle about the optical axis. The mirror can rotate to an angle of 8 degrees above the optical axis in order to view the cold of space for calibration and can rotate further, to an angle of 30 degrees above the optical axis, to view the warm in-flight calibration source. (See Section 7-4 for more details.)

As mentioned previously, the detectors are fixed in position within the detector capsule assembly of the cryogen cooler. Thus, these detectors are fixed relative to each other when the optics are scanning across the limb scene.

It is important when interpreting the data to understand the dimensions and spatial positions of the four channels. The FOV of the LRIR channels and their location relative to the limb scene are presented in Figure 7-7. The angular resolution (in milliradians) of each detector and their angular positions relative to each other are indicated. These angles correspond to the FOV at the radiometer. When this view is projected through the atmosphere at the limb, perpendicular to a vertical plane at the tangent point, the sampled area encompasses a rectangle that is 50 km in the horizontal by 20 km in the vertical. Within this area the O_3 and two CO_2 channels cover areas of 20 km and are positioned in a manner shown in Figure 7-7. The H_2O channel covers a much larger area, about 50 km by 2.5 km. However, due to excessive noise on the left side of

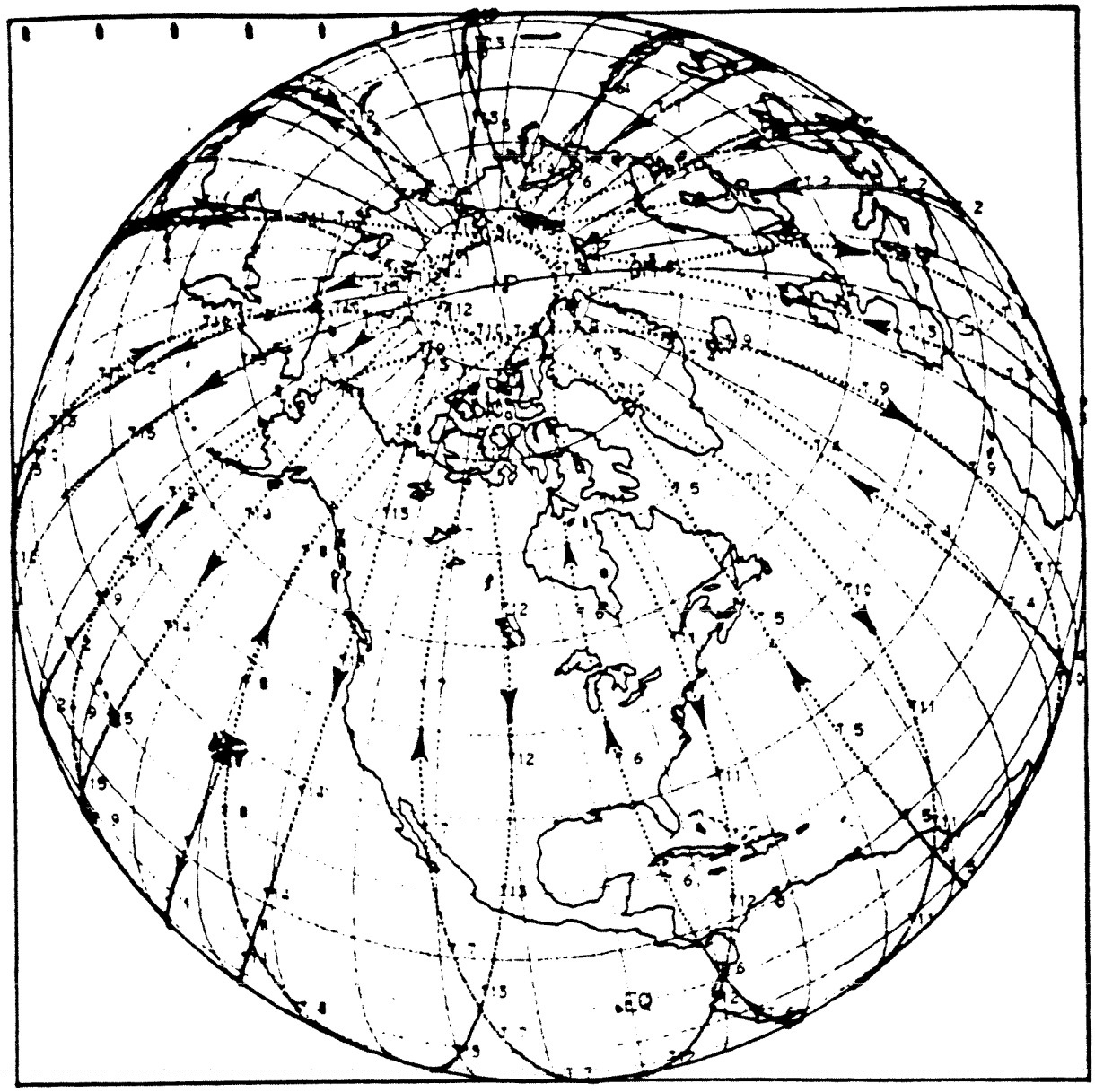

Figure 7-4. LRIR Scan Track for the Northern Hemisphere

channel 4, it was clipped and only the right side of that channel will actively acquire data. One can visualize this configuration as four narrow slits, parallel to the earth's surface and stacked one on the other as shown in Figure 7-7. For all practical purposes, observations by each channel are coincident in time and only slightly displaced from each other in the spatial domain.

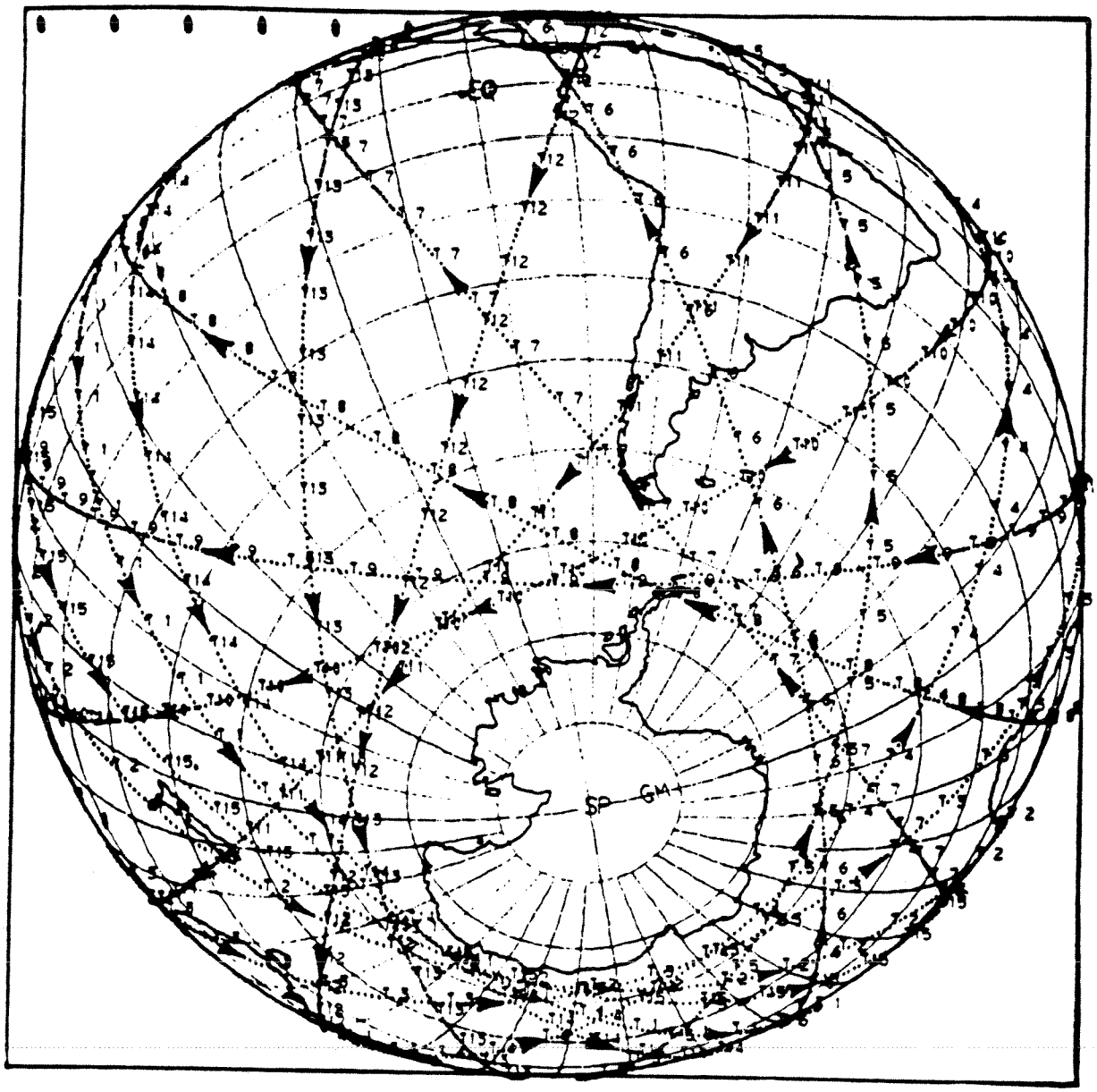

Figure 7-5. LRIR Scan Track for the Southern Hemisphere

The LRIR system block diagram is presented in Figure 7-8. The details of the diagram are self explanatory and illustrate information processing functions of both the FEU and IEU, shown in Figure 7-6.

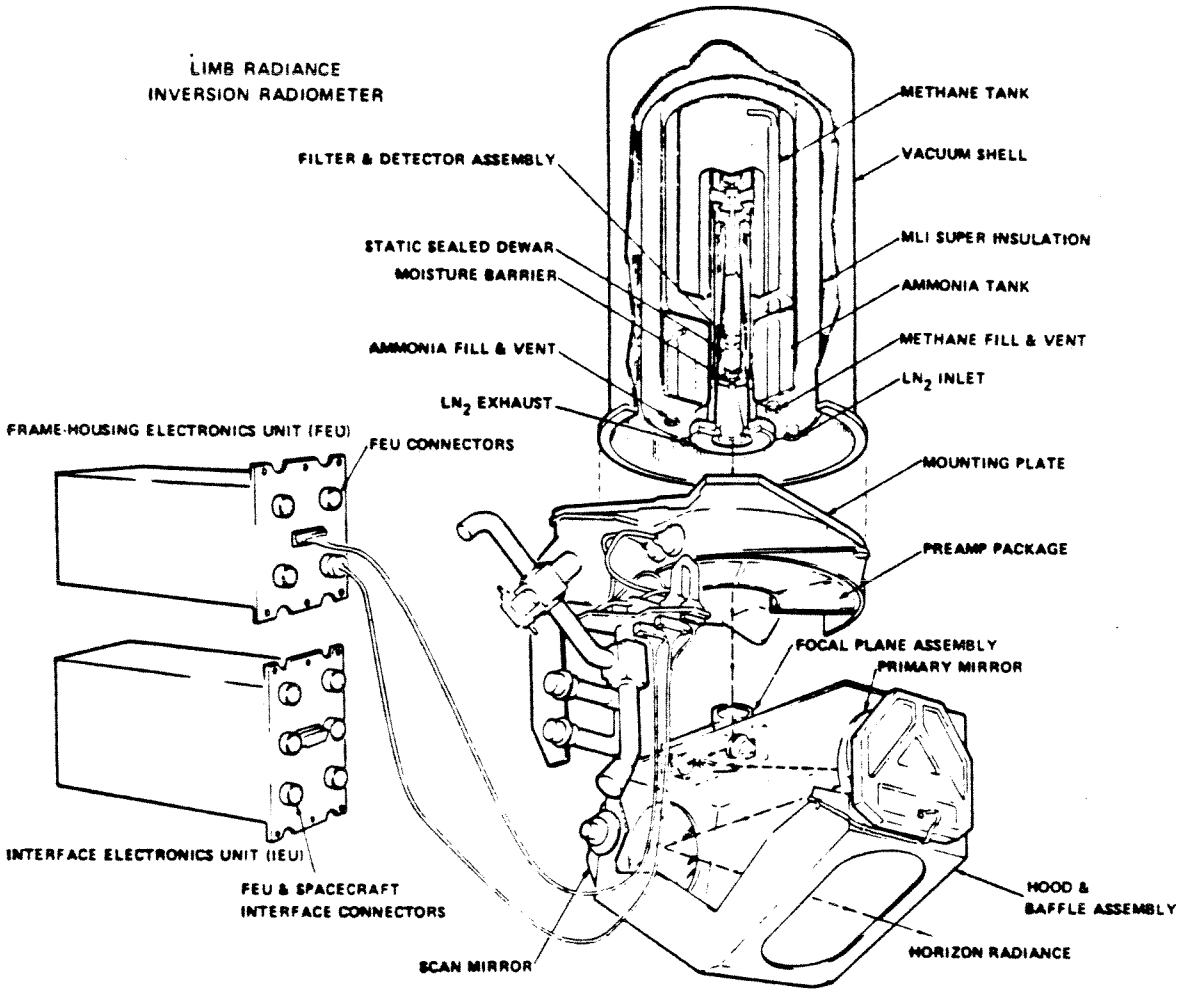

Figure 7-6. LRIR Instrument Configuration

7.3.3 Channel Characteristics

The optical characteristics of the four LRIR channels are presented in Table 7-2. Channels 1 and 2, the narrow (NCO_2) and broad (BCO_2) carbon dioxide channels, provide information on the temperature structure of the atmosphere. Channels 3 and 4 are the constituent channels for ozone and water vapor, respectively, and provide information on the vertical distributions of these trace gases.

Each channel of LRIR encompasses rather broad spectral regions about optical bands of their respective species of emitting gases. Since broad spectral

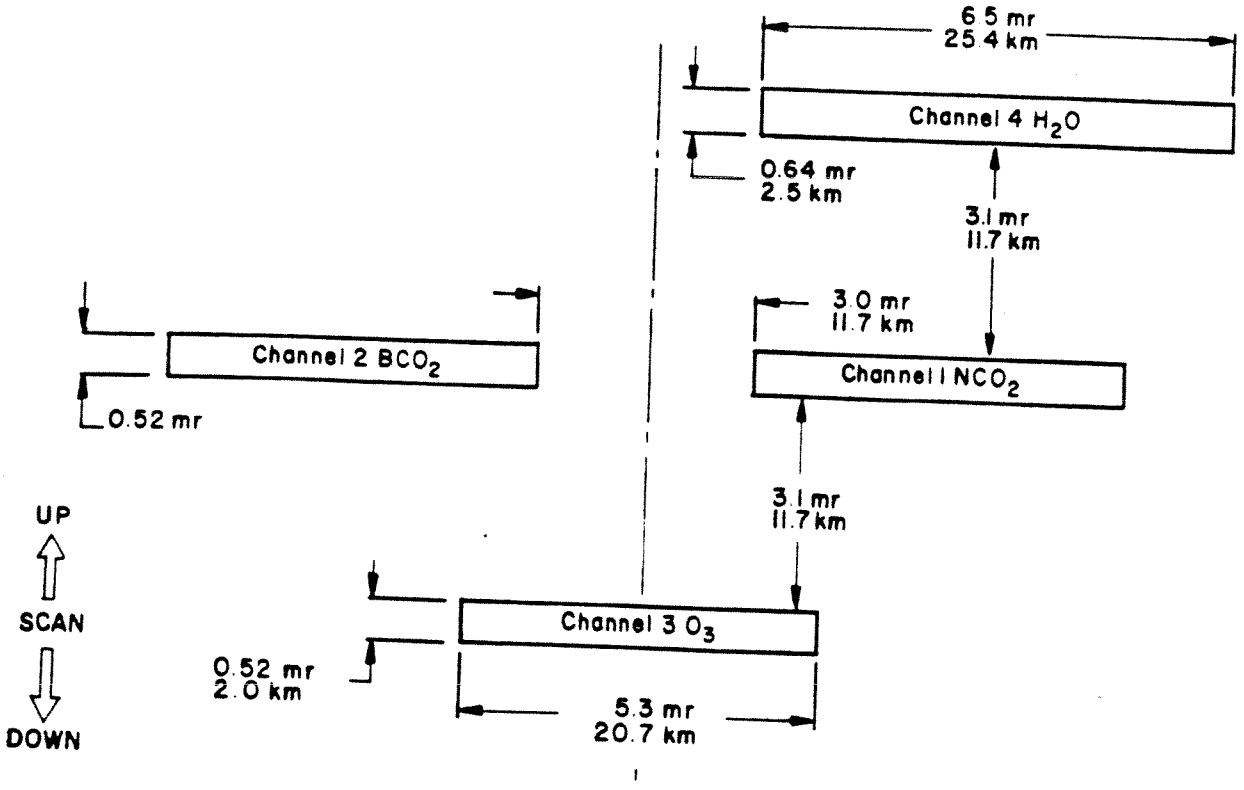

Figure 7-7. LRIR Field of View Dimensions. The IFOV arrangement is as viewed along the optical axis in the direction of the scene.

bands increase the magnitude of the received signal, the FOV can be reduced to the diffraction limit, and good vertical resolution can be obtained during the limb scan. Limb scanners use broad spectral bands with narrow angle FOV sensors to obtain altitude resolution. This philosophy of approach is different from nadir viewing experiments which employ narrow spectral bands with relatively large FOV sensors to accomplish altitude discrimination of information.

The location of the two CO_2 bands is not symmetrical about the 15 μm band center, but is shifted to the short wavenumber (long wavelength) side of the spectrum. This avoids contamination by the ozone band near 14 μm. Because each band provides a limb radiance profile (see Figure 7-2) of different character, both are utilized in the process of obtaining temperature inversion solutions. Together, they help to discriminate a unique solution to the problem (see Reference 1). Good data can be obtained solely from the BCO_2 channel when statistical inversion techniques are applied to the limb radiance data. However, temperature accuracy would degrade somewhat.

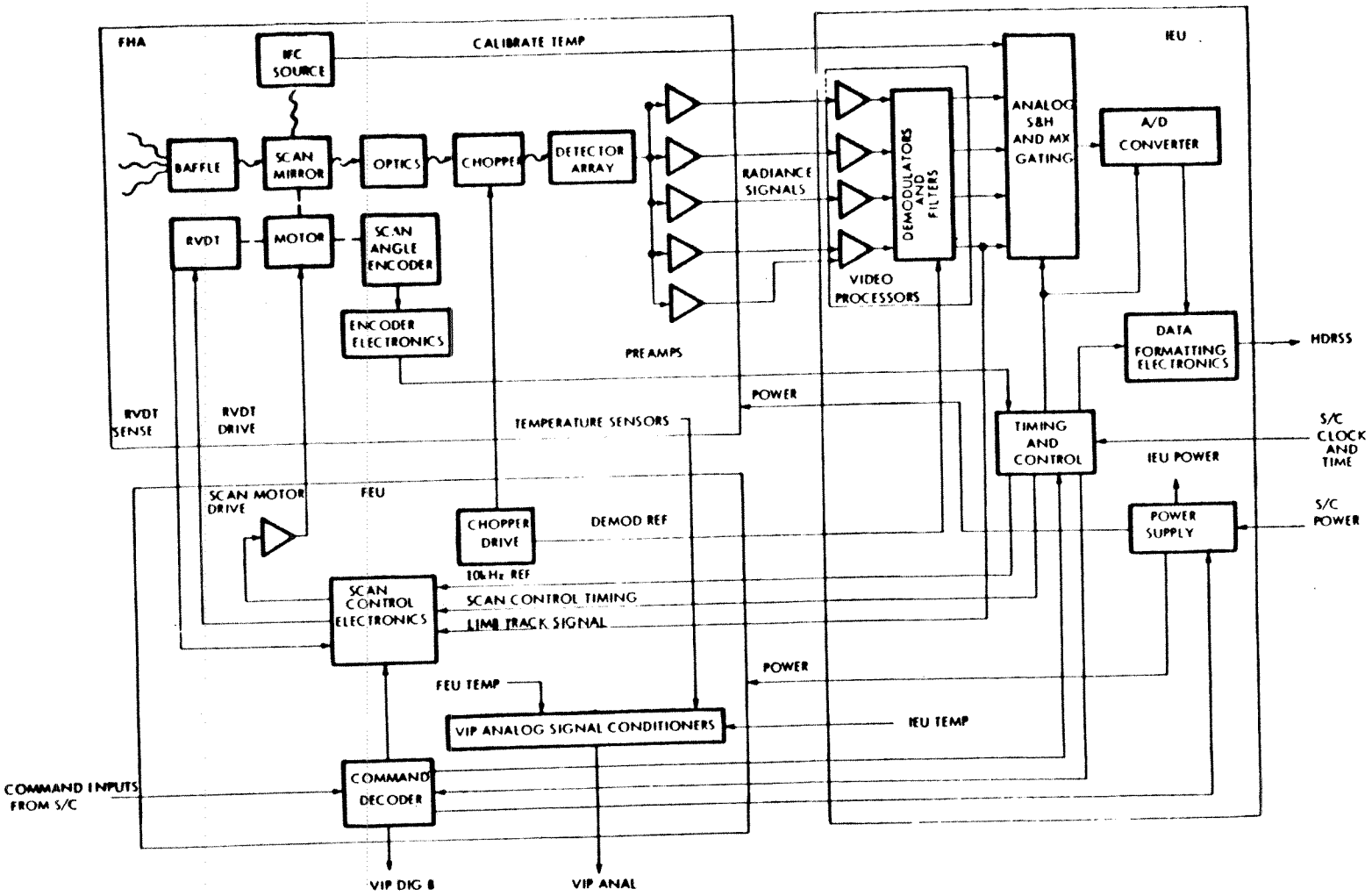

Figure 7-8. LRIR System Block Diagram

Table 7-2
Optical Characteristics of LRIR Channels *

Channel		Band Pass (50% Peak Response)	Field-of-view (km)		Random noise $\pm 1\sigma$ (watts/m^2 -sr)
No.	Abbrev.		Vertical	Horizontal	
1	NCO_2	645-670 cm^{-1} (14.9-15.5 μm)	2.0	20	0.0026
2	BCO_2	590-695 cm^{-1} (14.4-16.9 μm)	2.0	20	0.0046
3	O_3	980-1165 cm^{-1} (8.6-10.2 μm)	2.0	20	0.011
4	H_2O	370-435 cm^{-1} (23.0-27.0 μm)	2.5	25	0.021

The band pass for channel 3 (O_3) is centered at 9.6 μm to maximize the O_3 signal. The cuton wavenumber of 1165 cm^{-1} minimizes contamination by CH_4 and N_2O at 7.8 μm, while the cutoff location at 980 cm^{-1} minimizes the effects of longer wavelengths due to aerosol and HNO_3 emission.

For channel 4 (H_2O), the cuton location of 435 cm^{-1} was selected to minimize contamination by residual wing emission from CO_2 and HNO_3. The long wavelength side cutoff at 370 cm^{-1} was set by the spectral response characteristics of the detector.

Also shown in Table 7-2 is a summary of the FOV at the limb and the random noise (one sigma) of each channel. With reference to the data requirements in Table 7-1, channels 1 and 2 noise levels are well within desired specifications and channel 3 is at the desired specification. However, channel 4 is somewhat noisier than expected which diminishes the spatial resolution (both geographical and vertical) of the H_2O data.

7.4 Calibration

The LRIR has undergone extensive preflight calibrations in the laboratory under simulated flight environments to determine its geometric, spectral, and system responses to known magnitudes and positions of radiance sources. These calibration procedures were performed to an absolute accuracy approaching one percent.

*This table was revised following launch. See Section 2.2.

7.4.1 Preflight Calibration

The preflight calibration of LRIR may be summarized by the following five procedures.

- Determine optical characteristics of the in-flight calibration source (IFC) for all LRIR channels.
- Calibrate the encoder used to measure angular position of the plane mirror in scan space.
- Determine the response of the LRIR system to a variable blackbody radiance source for:
  - (a) Ten points over the dynamic range of all channels.
  - (b) Three different environmental temperatures of the spacecraft.
- Determine the spectral response of each LRIR channel.
- Determine the FOV response of each LRIR channel in the scan plane.

The first two procedures are critical to the absolute accuracy and interpretation of flight data. The IFC source provides a signal that establishes system response to a large (warm) radiance source. Absolute accuracy is possible only if the optical characteristics of the IFC are known and its temperature is monitored accurately. The second procedure establishes where the instrument is viewing at any time in relative scan space.

Primary calibration (see Figure 7-9) in the third procedure determines the response of all LRIR channels to varying radiance sources over the expected dynamic range of limb radiances, and for the range of possible LRIR-spacecraft temperatures anticipated for the mission. This calibration procedure establishes the linearity of instrument response to varying magnitudes of radiance signals. Once this response is established for the operating environment aboard the satellite, it is assumed to hold throughout the mission. Thus, only two calibration points are required during flight to determine absolute radiance values - a zero radiance signal (space view), and a large radiance signal (the IFC source). A linear response is assumed to hold between these two points.

The last two procedures are of less importance than the others in determining absolute radiances and their positions in scan space. However, these calibrations are important in the inversion process in understanding what is

Figure 7-9. LRIR Instrumentation During Primary Calibration

being observed optically across the band pass of each channel and how the limb radiance is being averaged spatially.

7.4.2 Scan Modes and In-Flight Calibration

The scan mirror subsystem operates in any of five scan-calibrate modes related to limb acquisition, limb scanning, and in-flight calibration. These five modes are listed below and functionally depicted in Figure 7-10.

- Acquisition Scan

  This scan generates a one degree per second line of sight (LOS) triangular sweep centered about OMP centerline. A complete period takes 20 seconds.

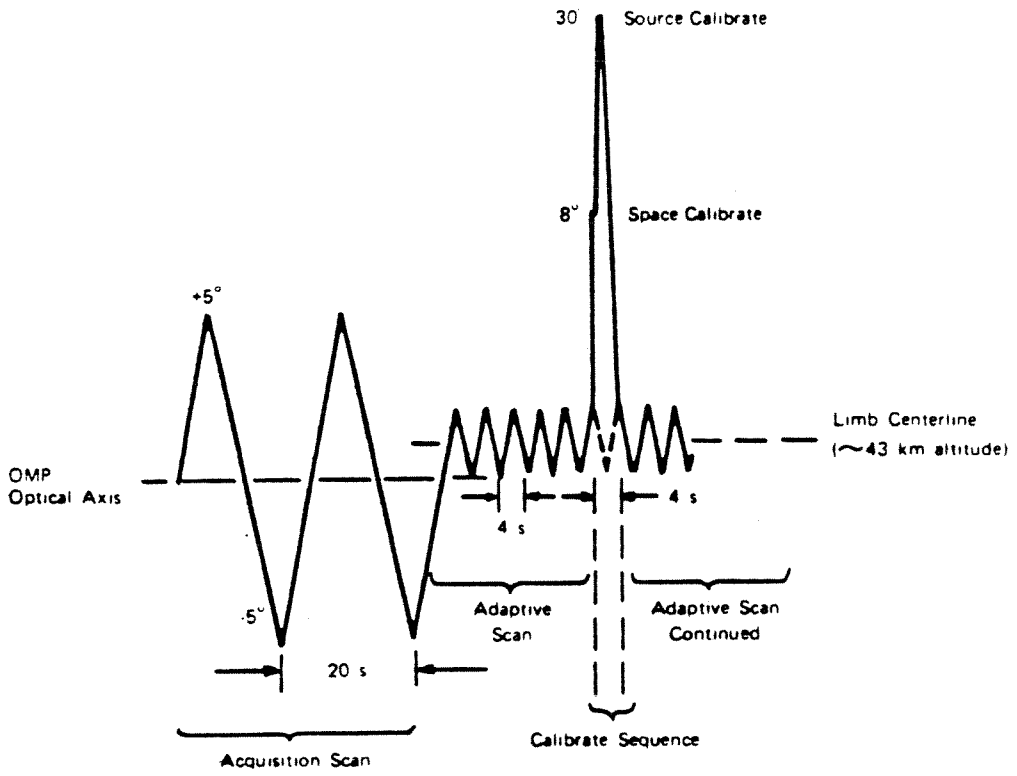

(a) LRIR Scan Modes - Angular Scale

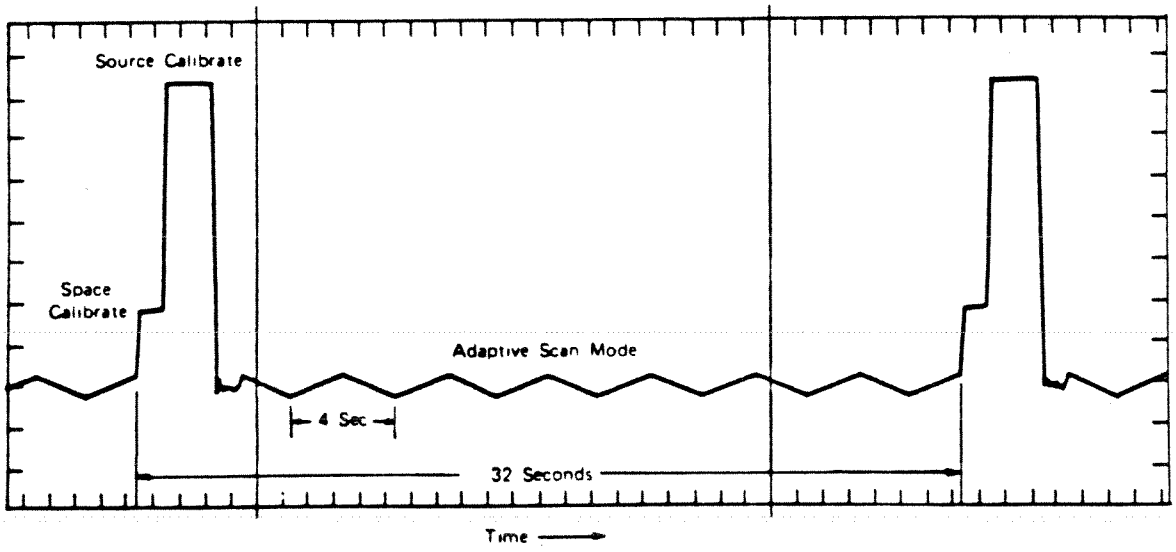

(b) Analog Trace of LRIR Adaptive Scan/Calibrate Sequence Modes

Figure 7-10. LRIR Scanning Modes During Limb Acquisition, Limb Scanning, and In-Flight Calibration Sequences

- Adaptive Scan

  This scan activates the Limb Tracking Circuit and generates a one degree per second LOS triangular sweep centered about 40 percent of the peak radiance of the narrow band CO_2 channel with a period of 4 seconds.

- Space Calibrate Hold

  This mode generates a dc voltage to position the scan mirror at a space calibrate position within ±1/2 degree shaft angle.

- Source Calibrate Hold

  This mode drives the scan mirror to a physical stop position to look back at the In-Flight Calibration Source (IFC).

- Automatic Calibrate

  This mode generates a calibrate sequence consisting of one second space calibrate hold dc level, a two second source calibrate hold dc level, and a one second return to OMP centerline to await the return to adaptive scan. This is an internally generated command.

Briefly, acquisition scan searches for the limb radiance within a ±5 degree arc about the OMP optical axis (see Figure 7-10a). Once the limb is acquired, the scan mirror subsystem switches to adaptive scan mode during which time limb radiance profiles are recorded over a ±1 degree scan about the limb centerline (a nominal 43 km altitude in the atmosphere). From a tangent at the earth's horizon, the range of altitude of the adaptive scan is between -25 km to 120 km. If the satellite attitude should change during successive limb scan periods (4 seconds for one down and up scan), the scan mirror will automatically adapt to the new limb centerline. This procedure continues during each limb scan period.

The automatic calibrate mode is activated during adaptive scan operation every 32 seconds while limb radiance data are being acquired. See Figure 7-10b for details. During the automatic calibrate sequence, the scan mirror rotates upward to an 8 degree angle above OMP centerline for a 1-second space (zero radiance) calibration and then to a 30 degree angle above the OMP centerline for a 2-second IFC source calibration before returning to the OMP centerline to await return to adaptive scan mode. The scan mirror can also be commanded to hold either the space calibrate or the source calibrate mode.

Section 2.2

POST-LAUNCH VERSION OF TABLE 7.2

(From the Nimbus 6 Data Catalog No. 2)

Post-launch analysis of relative spectral response data and orbital data leads to the following corrected values for Table 7-2, on page 154 of the User's Guide.

Table 7-2

Optical Characteristics of LRIR Channels

Channel		Band Pass (50% Peak Response)	Field-of-view (km)		Random noise in orbit* $\pm 1\sigma$(watts/m^2-sr)
No.	Abbrev.		Vertical	Horizontal	
1	NCO_2	649-672 cm^{-1} (14.9-15.4 μm)	2.0	20	0.0023
2	BCO_2	592-700 cm^{-1} (14.3-16.9 μm)	2.0	20	0.0040
3	O_3	984-1169 cm^{-1} (8.6-10.2 μm)	2.0	20	0.011
4	H_2O	412-446 cm^{-1} (22.4-24.3 μm)	2.5	25	0.008

***Noise will gradually increase as the detector temperature increases during the useful life of the experiment.**

2.3 INSTRUMENT PERFORMANCE

The instrument worked very well during its lifetime. The two stage cryogen cooling system maintained the detectors at the cold stable temperatures necessary for low noise measurements. The nominal preflight estimate was 65 K; however, the actual inflight environment was nearer 64 K until the beginning of January when the sublimation and eventual depletion of the methane became apparent. LRIR was shut off on January 8 at which

time the detector temperature exceeded 67 K. It was only in this final stage of operation that the noise levels exceeded specification. Measured radiances in both CO_2 channels had considerably lower noise than specified.

The scan mirror operated completely successfully, encountering no measurable bearing wear or other deterioration. This, in turn, contributed to the trouble-free operation of the inflight calibration system, to which the mirror returned every 32 seconds.

The data collection and recording system also functioned well. The A/D converter provided a continous noise-free 12 bit data stream to the on-board recorders. No extraneous signal, other than the expected random background noise has been detected at any stage in the data flow.

Those hardware problems that did arise after launch have proven quite amenable to correction in the software. The following sections provide a brief synopsis of these effects and indicate the software fixes required.

2.4 CALIBRATION

All calibrations are based upon the relative spectral response measurements. These were made without regard to polarization. It has since been learned that the Jarill-Ash Monochromator has an output whose polarization can be large, and is a function of frequency. If the LRIR is polarization sensitive, there could be undeterminable errors in the relative spectral response, and subsequently in the calibration. Based on present information, these effects are not anticipated to be of major importance.

The in-band blackbody radiances were calculated from the relative spectral response measurements and used in the primary calibration. A small, but significant S-shaped nonlinearity was discovered in the relationship between the radiometric output and input radiances, which was traced to the electronics. The nonlinearity was introduced in the form

$$V = V_o + A(N - \bar{N})[\,1 \pm r(N - \bar{N})]$$

where

V = output voltage

V_o = electronic offset, given from measurements of electronics

N = input radiance

$\bar{N}$ = input radiance corresponding to V_o (zero relative signal)

r = quadratic curvature term

From the primary calibration, r was determined for each channel, as described in MPRs.

The calibration curve was then used to determine the IFC radiance, which was fit by an expression of the form

$$N_{IFC} = \left[\varepsilon_{IFC}\, B_{IFC} + (1 - \varepsilon_{IFC})B_N\right](1 - \varepsilon_{IFC}) + \varepsilon_M\, B_M \qquad (2.2)$$

where

N_{IFC} = in-flight calibration radiance

ε = emissivity

B = Planck function

Subscripts: IFC = in-flight calibrator

N = radiometer housing

M = primary parabolic mirror

N_{IFC} and the space view (N = 0) were inserted in 2.1 to determine A and $\bar{N}$.

The temperature of the IFC, sampled at random through the experiment remained quite constant over the life of the experiment, at a value between 320.2 and 320.4.

The scale factors A for the 4 channels are shown for the period of the experiment in Figure 2.4a. They are quite steady, except for the end of the experiment, where they begin to decrease as the detector temperatures (Figure 2.4b) rise.

Channel 2 was frequently saturated when viewing the IFC during the first month, due to methane (and detector) temperatures being slightly lower than anticipated, and the instrument housing being cooler than expected. The ratio A_2/A_1 was plotted as a function of time for orbits for which data existed. A smooth function was drawn through those points, and used to determine A_2 during Channel 2 saturation.

2.5 NOISE

The standard deviation of the twenty-five space calibration values and of the 50 IFC calibration values were formed,

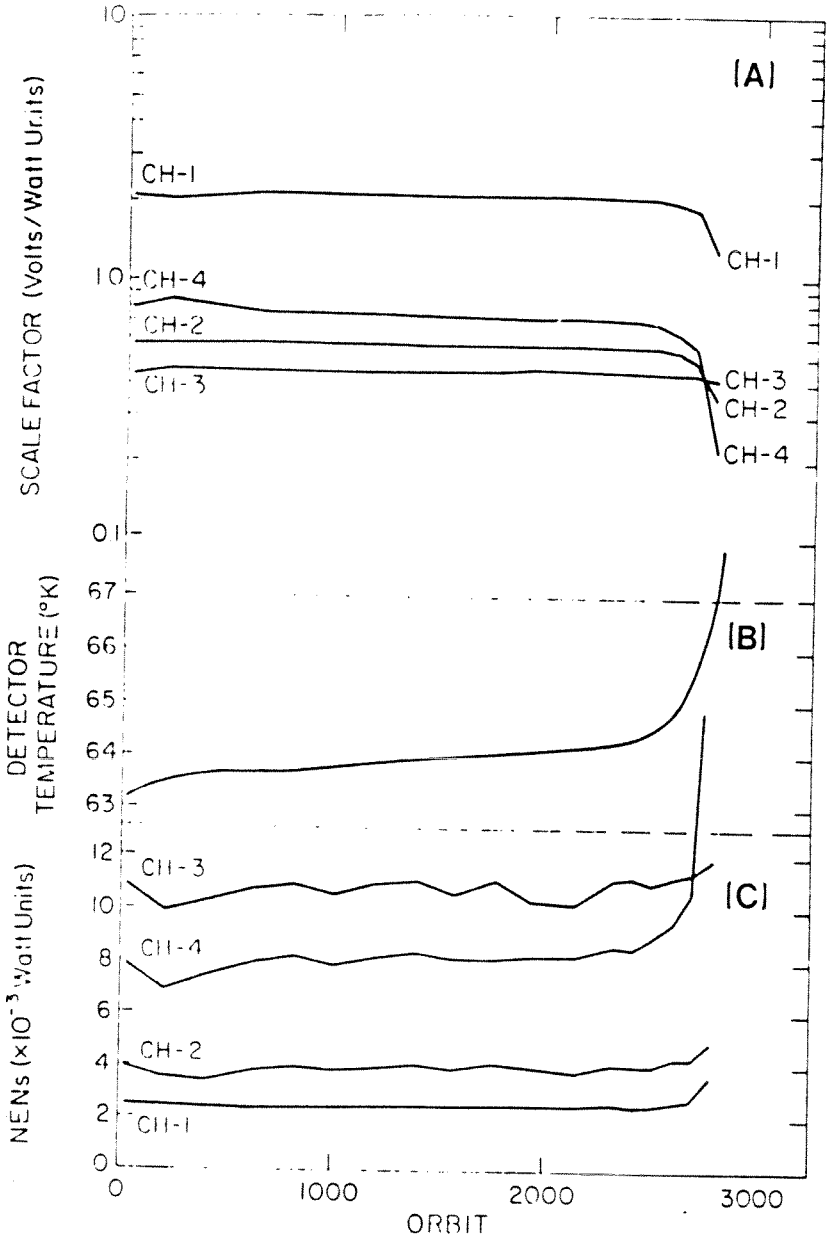

Figure 2.1 (A) Plot of the scale factors used to convert measured voltage to watt units as a function of orbit. All channel responses deteriorate rapidly with the onset of increased detector temperatures.

(B) Plot of the detector temperature as a function of orbit. The nominal pre-flight studies called for a detector temperature of 65 K.

(C) Plot of calculated noise equivalent radiance (NEN) for each channel as a function of orbit. Again the expected deterioration corresponding to the loss of cryogen can be seen.

and divided by A to give two estimates of the noise. The IFC noise values were generally somewhat larger than the space noise values. The mean of these values was taken as a best estimate of the instrument noise. Values over the life of the experiment are plotted in Figure 2.4c. The noise can be seen to be quite constant over the life of the experiment (except for the final period), and close to the preflight values. Note that the noise values in Channels 1 and 2 are below the specification of 10×10^{-3} by a factor of 3.

2.6 SCAN TOP CORRECTION

The possibility existed that there might be a small, angular dependence of the signal when looking at the uniform background of space. A block of acquisition scan data was obtained during Orbit 1610. Processing of these data indicated that there was a very small effect, of about 1 count per degree, roughly the same for all channels. This effect was deemed to be sufficiently small that the slope did not need to be removed, but the top of all scans (about 110 km altitude) was set equal to zero, and points below referenced to it.

2.7 ENCODER

In the adaptive scan mode, radiance samples were initiated by pulses generated by the shaft encoder mounted on the scan mirror. The nominal spacing of samples was 79.1 $\hat{s}$ line-of-sight (LOS). The 72 bit data word was processed into the 4 K bit data stream in 18 ms, with the remaining time until the next encoder pulse occupied by filler bits. The nominal number of filler bits was 17 with a scan rate variation of 20% allowed. If the succeeding encoder pulse occurred before the 72 bit data word was processed, a missed pulse flag occurred. If the next encoder pulse did not occur within 25 ms, a scan stop flag was set.

At the time of launch, the encoder had drifted significantly from its state as measured during the encoder mapping scans. By August 1975, the symmetry of the square waves generated by the encoder drifted to the point that approximately 25% of the encoder pulses occurred before the processing of the previous 72 bit word was completed. This resulted in the loss of 25% of the data. Recovery from both conditions, encoder drift and data loss, was possible through sophisticated software as described in Section 3.

2.8 INTERNAL REFLECTION (CROSS TALK)

Shortly before launch, inspection of some earlier laboratory scans across a steep ramp demonstrated that trailing channels responded when leading channels began to measure the rising signal from the ramp.

Subsequently, in orbit, LRIR viewed the moon on two occasions as it set behind the atmosphere. These data showed two qualitative effects, i.e.,

1. The effect was still present, in orbit; and

2. The effect resulted from spatial mixing, but not spectral plus spatial mixing. This conclusion resulted from the continued effect of the O_3 and CO_2 channels positions of the H_2O channel signal, even after the moon's direct signal on the O_3 and CO_2 channels were filtered out by atmospheric opacity.

Subsequently, a simular effect has been measured on the LIMS instrument during the hot wire IFOV measurement. These data also indicate the shape and half-width of these side lobes.

The solution has now been to use a cross talk model having side lobe locations determined by positions of the field of view mask, shapes taken from LIMS measurements, and magnitudes determined from the moon observations. Present application of these corrections will be described below in Section 5.

2.9 WATER VAPOR CHANNEL

These are several problems with the water vapor channel, Channel 4.

1) Because of detector problems, the cutoff wavelength occurs below 25 μm rather than beyond 27 μm, as specified. Because there are several strong clusters of water vapor lines between 25-27 μm, received signals are considerably less than expected. Although noise levels are approximately 0.008 W m^{-2} sr^{-1}, below the specified 0.01, the signal to noise ratio is worse than expected.

2) Because of the reduced water vapor signal, emission from the long wavelength wing of a nitric acid band at 22 μm contributes signal comparable to the water vapor in the 25-30 km altitude region. The extent to which they can be separated is not clear.

3) Perhaps most seriously, at levels above 30 km, Channel 4 measured radiance is greater than that calculated for reasonable water vapor distributions by factors of 3-6.

The reasons are not clear at this time. Candidate explanations include incorrect or temperature dependent spectral response, cross talk effects, decalibration effects or perhaps something else.

Section 3

LRIR DATA PROCESSING

3.1 Input Data

The intermediate data products in the LRIR data processing scheme are the Radiance Tapes (RT). The process flow for RT production is shown in Fig. 3.1. The input data streams necessary for the production of RTs consisted of the LRIR Data Tapes (LDT) and the User Formatted Output Tape (UFOT). The LDT contained the radiance channel output voltages and some housekeeping data interspersed with time code data. The UFOTs contained the LRIR analog output, spacecraft status information attitude control system (ACS) outputs, and spacecraft ephemeris data. Due to a variety of errors frequently found in the LDTs and UFOTs, an edit process was applied to each before further processing.

In the UFOT data stream most of the detectable errors occurred in the time field, so it was checked and edited first. Time spikes and misordering were detected and either corrected or removed. Using the corrected time field as a base, other variables which varied as a predetermined function of time along the orbit track (latitude, longitude, altitude) were then checked, and obvious errors removed by interpolation. Finally the remainder of UFOT major-frame data were checked.

Errors entered the LDT data stream from two sources. The most frequent was the occurrence of noise somewhere in the data transmission link or initial telemetry processing which produced spurious sync patterns, mode bits and data spikes. The second class was a result of logic errors associated with the encoder electronics within the instrument which led to false mode indications and occasional bad time codes. If

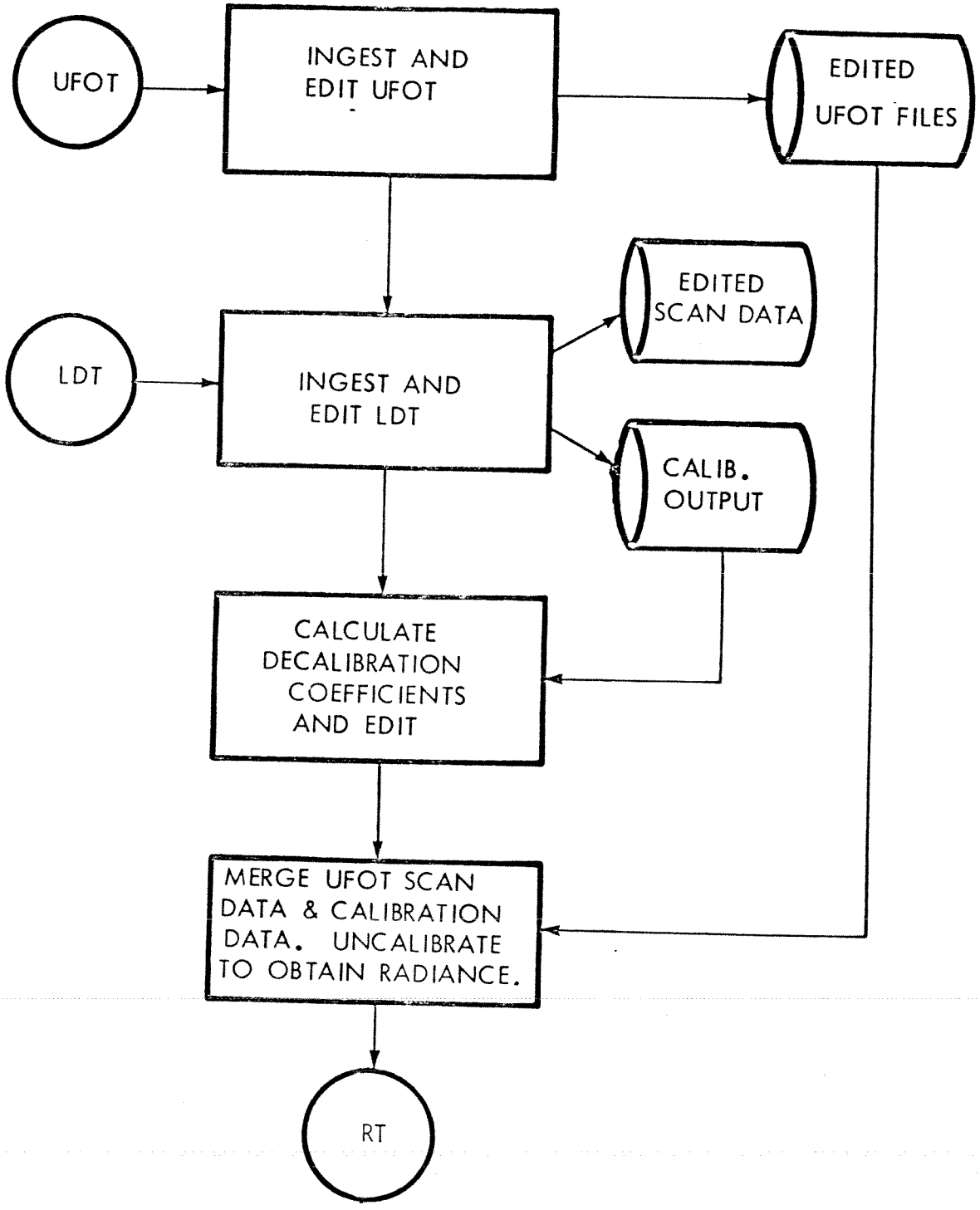

Figure 3.1 Conceptual process flow chart giving an overview of RT production from UFOT-LDT input.

these errors resulted in anomalies in the calibration cycle, the data were discarded. The radiance channel outputs were then checked for spikes and corrected if possible. Any anomalies encountered in the edit procedure were noted both as to type and location within the scan and this information became part of the edited scan data records.

The production of RTs basically consisted of merging the two data streams in time, extracting the radiance outputs associated with the inflight calibration sequence, calculating the calibration coefficients and applying the resulting decalibration equations to the scan data. The data were located geographically by interpolating the spacecraft ephemeris data in time to correspond to the time of the scans and then calculating the location of the tangent point at that time using the known orientation of the instrument line-of-sight to the spacecraft axes.

At the time of launch, the encoder had drifted significantly from its measured pre-launch state, resulting in improper location of the samples. By the second month of the experiment, the encoder had further shifted to the point that 25% of the pulses occurred too late for the sampling electronics, resulting in data loss. Because some properties of the encoder are relatively invarient, it proved possible to recover from both the drift and the data loss through sophisticated software.

Due to inability to accurately calibrate the water vapor radiances, no inversion of the radiances was performed.

The RT then contains radiance values for each channel, angular separation between samples, error diagnostics, housekeeping data, spacecraft and tangent point location for the scans. A calibration cycle record occurs between every seven scan records, containing the decalibration coefficients and relevant housekeeping data.

3.2 Inverted Profile Archival Tape Production

3.2.1 Overview

The Inverted Profile Archival Tape (IPAT) represents the level of LRIR archival products. It contains the inverted profiles as a function of pressure at selected latitudes as well as the radiances corrected for instrumental and spacecraft effects which were used in the inversion process. The program which creates the IPAT has eight major divisions:

- The input of Radiance Tape records
- The application of selection criteria for determining which profiles will be inverted
- The removal of spacecraft motion and spacecraft attitude effects
- The removal of instrument effects and data smoothing
- The determination of cloud tops
- A first guess inversion for determining a basic reference in pressure
- A final detailed inversion
- The formatting and output of IPAT records

3.2.2 Input and Unpacking of RT Records

The number of RTs, the tape identification for each RT and the number of orbits on each RT are read as input data cards at the start of each IPAT run. The program keeps track of the status of each tape and issues a call for each tape volume as needed.

As the RT records are read, the number of words in each record is checked to determine if it is a profile pair record or a calibration cycle record. In the present version of the software, the calibration

cycle records are ignored. The profile pair number in the scan-calibration sequence is noted. Pair 7 which contains scans 13 and 14 in the sequence is ignored because scan 14 is not a full scan. The input subroutine works in conjunction with the profile selection part of the program. Initial calls to the input routine result in an input record being read and identified. If the record is a profile pair record, the spacecraft and tangent point locations only are unpacked. These parameters as well as the packed data record are returned to the calling part of the code. If the record is selected for further processing, a second call to the input routine will unpack the record into radiance profiles and perform some basic quality checks. If any of the quality checks fail, a flag will be passed to the calling subroutine.

3.2.3 Selection of Profiles for Inversion

The profile selection section of the program has two options for selecting profiles for inversion. For the production of IPATs, the program selects the closest "good" profile pair to specified standard latitudes. These have been selected to be 4 degree latitude increments, from 64°S to 84°N. The second selection mode is used to find specific overpass situations; it picks the closest good profile to specified latitude and longitude points that fall within selected windows.

In either selection mode, the software performs a variety of quality control checks on the input radiance data as well as the ongoing processing. If a problem with a profile is detected or if a parameter is falling outside a specified tolerance, the program goes back and begins again with the next closest "good" profile. If it is the case that no acceptable profile exists within the specified windows, a diagnostic message is printed to this effect.

3.2.4 Removal of Spacecraft Motion and Attitude Effects

Spacecraft motion in the scan plane tends to compress or expand the actual spacing between sample points at the horizon from that determined by the encoder. If the actual local spacecraft rate is known the angular reference can be altered to account for it. However, the outputs of the ACS are inadequate for determining this to the necessary accuracy ($\leq 0.005°/s$).

To accomplish this, the LRIR data must be used. At the scan rate of 1°/s over a 2° scan, the spacecraft travels a distance of about 12 km at the earth's surface between the centers of successive down and up scans. The horizontal averaging distance along the ray path is about 250 km and the width of each of the CO_2 channels is about 20 km. The total width of the field of view is 52 km between the outer edges of the CO_2 channels. Hence the averaging scales are much larger than the sampling scales. Also the spatial scales for significant meteorological variability are greater than 12 km. Hence, to a very good approximation the radiance profile observed on a down scan should be the same as that on the up scan to within the system noise. Any large scale differences in shape should be attributed to spacecraft motion distorting the profiles in different ways.

Two basic assumptions are made in correcting the LRIR profiles.

(1) The atmospheric radiance profile is the same between successive down and up scans;

(2) The spacecraft motion is constant over this period (no acceleration).

A constant multiplier is found which best fits the angles on the down scan to those on the up scan in a least squares sense. The effect of the constant spacecraft motion on the up scan is opposite to that on the down scan, and the stretching or compression determined is twice that actually present. The true angular scale is obtained by picking an arbitrary point as the point of zero stretch and applying the calculated stretch factor in opposite senses on either side of the point. At the end of the process the up and down scans are on the same angular scale and are merged to form a composite radiance profile. At this point the spacing between points is not uniform.

A second attitude effect is the slight offset effect of the wide CO_2 to the narrow CO_2 channel due to a "twist" about the bore sight. This may be calculated to within a constant offset by transforming the ACS data from the spacecraft axes to the sensor axes. The magnitude of the constant offset was selected empirically by conducting sensitivity studies.

3.2.5 Removal of Instrument Effects and Data Smoothing

A slight bias (about 1 NEN) exists on the space view side of the radiance profiles due to a small angular dependence of the output. This is removed by averaging several points at the top of the scan where the radiance is very close to zero, and removing this amount from every point on the merged profile.

The next step is to remove the effects of the field of view from the radiances, particularly those due to off axis reflection or "cross talk". This is accomplished most efficiently by the application of Fourier transforms in conjunction with the convolution theorem. Data

from the merged profile is linearly interpolated to the angular equivalent of 0.75 km spacing. The ends of the profiles are artificially extended and padded with zeros to prevent end around leakage and to make the number of data points a power of two (512). To insure proper band limiting and to achieve desired smoothing of the radiances, a low pass filter is applied to the data before the inverse transform is taken. The deconvolution accomplishes two things. First, the effects of "cross talk" are removed. Second, since the IFOVs are all referenced to a common spatial origin (the top of the focal plane array), the inherent offset of one channel to another is removed so that radiance points in each channel are registered at the same relative angles when the transform back to measurement space is performed. After the inverse transform takes place, every other radiance point is taken so that the resulting spacing of points in the inversion is 1.5 km in apparent tangent height.

3.2.6 Determination of Cloud Top or Lower Inversion Limit

Normally 40 radiance values are taken for the temperature inversion. The actual lower limit for the inversion is 100 mb or cloud top whichever is higher in altitude. To determine if a high cloud is present in the lower portion of the scan, the retrieval ozone values are examined for abrupt changes in slope.

3.3 Retrieval Algorithms

The underlying physical principles of infrared limb scanning and methods for interpreting such measurements have been described by Gille and House (1971), Russell and Drayson (1972), Gille and Bailey (1977), Bailey and Gille (1978) and Gordley and Russell (1981). The following description of the LRIR inversion is based on Bailey and Gille, 1984.

The basic approach is to deduce the vertical temperature and pressure profiles of the atmosphere from observations of thermal emission by a gas whose concentration profile is known and for which the radiative transfer can be modeled. In the case of LRIR, this was done using two channels in the 15 μm CO_2 band. Once the temperature and pressure profiles are known, the vertical concentration profiles of ozone can be determined from measurements of its thermal emission at 9.6 μm. This requires the ability to model the radiative transfer for the spectral intervals in question, including the effects of any contaminating emissions which may be present.

Retrieval algorithms for remote sensing applications have been the object of considerable research both from the standpoint of mathematical theory and physical application. This work has been well summarized by Rodgers (1976) and Twomey (1977) and will not be reviewed here. Almost all of the work has addressed the stability of algorithms in the presence of observational errors. While this is important, it is only one consideration in the design of an operational algorithm. Other aspects which must be considered include: the degree of nonlinearity, ease of implementation, maintainability, adaptability, and cost when applied in a production environment. Each of these points has, to some extent, dictated the algorithm described in this section.

3.3.1 Forward Radiance Model

As implied earlier, the ability to accurately calculate the limb radiance for a given atmospheric state and set of instrument parameters is an essential prerequisite to doing useful retrievals on data obtained by that instrument. The philosophy maintained throughout this interpretation of LRIR measurements was to rely as much as possible on physical first principles and to avoid empirical adjustment. Thus, discrepancies between observations and theory or correlative measurements have been explained or accounted for in terms of instrument behavior or the radiative transfer physics giving rise to the signal.

Several simplifications can be made to the radiative transfer equation for infrared limb emission applications. In the wavelength and altitude regions of interest, the effects of scattering may be neglected. For the limb geometry, the boundary term may be eliminated since the background is cold space. The radiance observed by a real instrument looking in the direction θ is then

$$N(\theta) = -\int_{\theta_1}^{\theta_2} \int_{\nu_1}^{\nu_2} \int_{s=0}^{s=\infty} B\{\nu, T(s)\} \frac{d\tau}{ds} (\nu, \theta', s)\, F(\theta'-\theta)\, R(\nu)\, ds\, d\nu\, d\theta' \quad (1)$$

where

$B\{\nu,T(s)\}$ is the Planck function for frequency ν and temperature T at point s along the ray path.

$\frac{d\tau(\nu,\theta',s)}{ds}$ is the derivative of the transmittance

$F(\theta' - \theta)$ is the effective field of view function of the instrument which is nonzero for

$\theta_1 < \theta' < \theta_2$.

$R(\nu)$ is the spectral response of the instrument which is nonzero for $\nu_1 < \nu < \nu_2$.

Refraction effects along the ray paths become significant for tangent heights lower than about 25 km and must be incorporated into the model. The primary difficulties, however, arise with the specification of the atmospheric transmittance. These difficulties include: extreme variation of transmittance with frequency due to spectral line structure; large variation in spectral line shape over the altitude region of interest; and the specification of the combined transmittance of several absorbing gases within a given wavelength interval defining a channel.

A synopsis of methods for parameterizing transmittance has been presented by Rodgers (1976). In the case of LRIR, transmittance functions for the primary emitting molecules in the CO_2 and O_3 channels were derived from line-by-line calculations for inhomogeneous limb path conditions. These high resolution transmittances were then averaged over broader spectral intervals and empirically fit as polynomials in terms of Curtis-Godsen type parameters (see Rodgers, 1976) which described the inhomogeneous paths. The method of fitting was similar to that described by Smith (1969). The transmittance models were developed at 5 cm^{-1} resolution to be compatible with the scale of changes in the instrument spectral response function, and yet retain the multiplicative property of transmittance in a mixture of absorbing gases.

In the numerical modeling of horizon radiance profiles, the integral form of Eq. (1) is replaced by a numerical integration formula consisting of finite sums over discrete spectral intervals and calculated at infinite vertical resolution.

$$I(\theta) = \sum_{i=1}^{N} \sum_{j=1}^{m} B(\bar{\nu}_j, T_i)\, \bar{R}_j\, \Delta\tau_{ij}(\bar{\nu}_j, \theta)\, \Delta\nu_j \qquad (2)$$

where the overbar indicates an average value over 5 cm^{-1} intervals. In the model, the atmosphere was divided into shells 5 km thick from 110 km to 90 km and 1.5 km thick from 90 km to the lowest tangent height of interest. Within each shell, temperature and mixing ratio were assumed to vary with a constant vertical gradient. For this approximation, the integrated absorber amount for a gas within the shell can be expressed algebraically in terms of the pressure, temperature and mixing ratios at the shell boundaries. The total path integrals are then sums of the shell integrals. This eliminates the undesirable assumptions of isobaric, isothermal or constant mixing ratio shells and permits calculations to the desired accuracy with relatively fewer vertical grid points.

The radiance model just described is capable of high accuracy but is too time consuming for use in an operational context. This model was used to develop a parameterization which will be described later. Spherical symmetry was assumed in the calculations used to parameterize the transmittance data base for the retrieval calculations.

3.3.2. Determination of Initial Temperature Solutions

In most situations, no absolute pointing information is available with which to reference a given radiance value to a particular tangent height. It then becomes necessary to identify some approximate pressure location at which to begin the inversion. At the same time, it is necessary to have an initial estimate of the atmospheric state with which to start the non-linear inversion process. If the retrieval algorithm is capable of fully handling the non-linear aspects of the problem, the initial solution need not be particulary close to the correct solution. However, a full treatment of the non-linearities generally leads to a more complex and expensive calculation scheme. In addition, iterative solutions can generally be obtained more economically and reliably if the starting solution is close to the true solution. It is therefore desirable to have a method to obtain such a profile in an inexpensive manner.

In the early studies of the limb radiance problem, it was recognized that a simple first order inversion method could be formulated based upon the highly localized nature of the weighting function (House and Ohring, 1969). This assumption provided the motivation for the corrector equation in the iterative scheme used by Gille and House (1971).

House and Ohring (1969) suggested a simple approximation in which the radiance at a tangent height h is approximated by

$$N(h) = \bar{B}\,[T(h)]\;\varepsilon(h) \qquad (3)$$

where

N(h) is the radiance

$\bar{B}[T(h)]$ is the spectrally weighted black body radiance for the channel

T(h) is the temperature

$\varepsilon(h)$ is the effective atmospheric emittance.

If the emittance is known, the temperature may be recovered from the Planck function. If a constituent mixing ratio is sought, the temperature must be known as well as a relationship between emittance and concentration. Thus a "direct" solution may be made for the parameter of interest without a full inversion of the radiative transfer equation.

For an isothermal, constant mixing ratio atmosphere with constant absorption, an idealized emittance may be derived similar to that given by Burn and Upplinger (1970)

$$\varepsilon(P(h), W, T) = 1 - \exp\left(\frac{-K\,P(h)W}{\sqrt{T}}\right) \qquad (4)$$

where P(h) is the pressure at tangent height h, W is the mixing ratio, T is the temperature, and K incorporates the constant absorption coefficient and other constants required for dimensional consideration. The radiance at tangent height h can then be approximated by the form

$$N(P(h)) \simeq \bar{B}[\hat{T}(h)]\left[1 - \exp\frac{-K[P(h)]P(h)\hat{W}(h)}{\sqrt{\hat{T}(h)}}\right] \qquad (5)$$

where the variables $\hat{T}(h)$ and $\hat{W}(h)$ represent temperature and mixing ratio averaged in some manner over the region of the atmosphere from which the radiance arises. A reasonable definition can be made by assuming that all the radiance comes from within one scale height H of the tangent point,

$$\hat{T}(h) = \int_{h}^{h+H} T(z)A(z)dz \Big/ \int_{h}^{h+H} A(z)dz \qquad (6)$$

$$\hat{W}(h) = \int_{h}^{h+H} W(z)A(z)dz \Big/ \int_{h}^{h+H} A(z)dz$$

Here A(z) is an arbitrary weight depending upon the optical characteristics of the atmosphere in the vicinity of h. The simplest assumption is that the weighting function A(z) is the normalized contribution function in the region h to h + H.

The effective absorption coefficient is difficult to specify accurately from first principles and could most easily be obtained empirically from detailed forward radiance calculations. The most useful form, however, is to specify effective emittance directly in terms of the atmospheric variable of interest and thus avoid the use of an absorption coefficient altogether. For this purpose, the emissivity is defined as

$$\varepsilon(P, \hat{T}, \hat{W}) = \frac{N(P)}{\bar{B}(\hat{T})} \qquad (7)$$

In the case of CO_2, the mixing ratio profile is assumed to be globally uniform and does not need to be considered explicitly. Temperature variability also appears to be of second order importance and can be neglected as an explicit parameter. This results in a simple relationship

$$N(P) = \bar{B}[\hat{T}(P)]\ \varepsilon(P) \qquad (8)$$

where $\bar{B}(\hat{T})$ is the instrument response weighted Planck function, which may be parameterized and inverted to give $\hat{T}(\bar{B})$. The $\varepsilon(P)$ are determined from (7) by calculating N(P) and $\hat{T}$ (using Eq. 6) for a set of atmospheres. Effective emmisivities for channels like the LRIR narrow CO_2 and wide CO_2 channels are shown in Figure 3.2. The effective emissivities for midlatitude

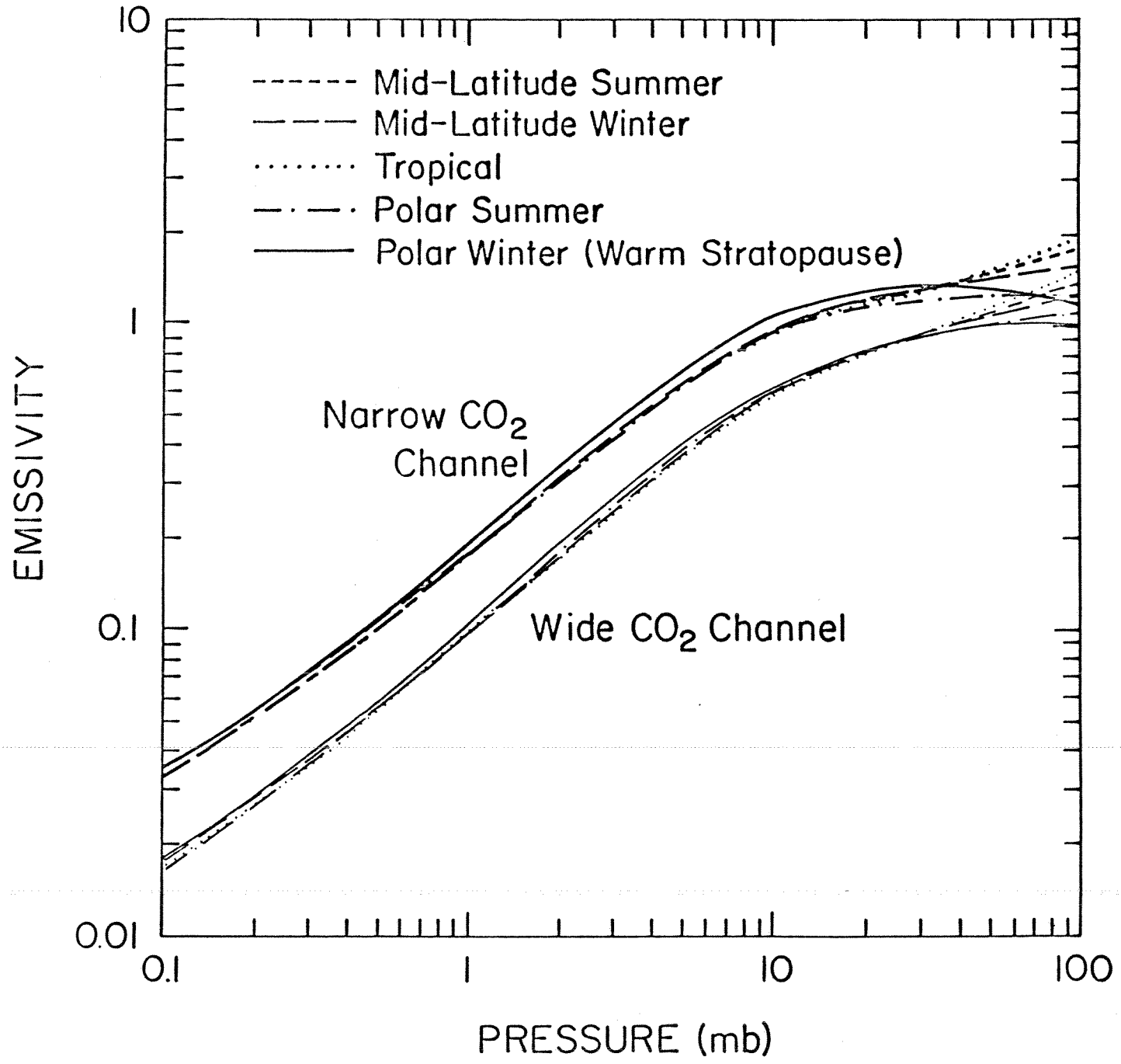

Figure 3.2 Effective total path emissivities for channels like the LRIR narrow and wide CO_2 channels.

and tropical atmospheres fall very close to the same curve. The cold polar and warm polar situations deviate most. It can be seen that values for the effective emissivity become greater than one as the channels become opaque. This is due to the assumption that all of the emission comes from within one scale height of the tangent point. In reality, the effective temperature for these pressures should be derived from a layer of the atmosphere greater than one scale height which is appreciably warmer than the region near the low altitude tangent points.

In application, the CO_2 radiance will not be known as a function of either temperature or pressure. Both parameters must be determined from observations made in two different spectral channels in the 15 μm CO_2 band having different optical properties.

Depending upon the averaging function A(h, z) used in Eq. (6), the $\hat{T}(P)$ profile may be inverted to obtain an estimate of the T(P) profile. Mathematically this is a simple operation since the equivalent matrix is banded. The process may also be iterated to provide a better $P(h_o)$ value.

As can be seen in Figure 3.2, the effective emissivity does depend to some extent upon the atmospheric situation being observed. This is accounted for in application by defining a set of climatological temperature profiles which adequately cover the range of atmospheric variability as well as a procedure by which the appropriate emissivity curves can be assigned to a particular observation. This is accomplished by classifying the observed radiance profiles according to latitude and season and comparing the observed radiances to a set of precomputed radiances appropriate to the situation. The emissivity curves corresponding to

the atmosphere whose normalized radiances best fit the normalized observed radiances are then used in the inversion.

A good initial altitude registration is obtained as a by-product of the fitting of observed to calculated radiances in the emissivity selection step. The use of the emissivities can be made somewhat implicit by ratioing the observations and the calculations for known atmospheric conditions. This has the effect of reducing the sensitivity of the retrieval to initial vertical registration errors. In forming the ratio of an observed radiance profile to a precalculated radiance profile using Eq. (8) we have

$$\frac{N_o(P)}{N_c(P)} = \frac{B(\hat{T}_o)\ \varepsilon_o(P,\hat{T}_o\hat{W}_o)}{B(\hat{T}_c)\varepsilon_c(P,\hat{T}_c\hat{W}_c)} \quad . \tag{9}$$

Where the subscript "o" refers to conditions corresponding to the observation and the subscript "c" to conditions calculated from climatological conditions.

At some reference altitude z_o, we assume

$$P(z_o) = P_c(z_o) = P_o \quad . \tag{10}$$

so $\varepsilon_o(P_o) = \varepsilon_c(P_o)$

The observed temperature can be estimated by an inverse table look up of $\hat{T}$ versus $B(\hat{T})$ where

$$B(\hat{T}_o(P)) = B(\hat{T}_c)\ N_o(P)/N_c(P). \tag{11}$$

P(z) is obtained recursively by using the hydrostatic equation starting at $P(z_o)$. The derived temperature at a point and the known spacing of

the radiance measurements are then used in the hydrostatic equation to obtain P at the next point, from which $\varepsilon(P)$ and its temperature are obtained. The solution then proceeds up and down from z_0.

Emissivity curves for sixteen atmospheric profiles were used in the processing. These were grouped according to the following classifications:

- mid-latitude winter
- mid-latitude summer
- tropical
- polar summer
- polar winter
- polar spring
- polar autumn

For a particular radiance profile, read in from the LRIR RT, the day of the year and latitude were used to choose one of the seven classes. The observed wide and narrow CO_2 radiances were aligned with the calculated profiles for that particular class by a least squares fit and the emissivity curves for the best fit situation were used to obtain the initial solution directly in the manner described above.

3.3.3 Determination of the Initial Solution for Ozone Mixing Ratio

An initial solution for mixing ratio may be estimated in a way similar to that for temperature. In this case, the effective emissivity of Eq. (7) is assumed to be an explicit function of mixing ratio

$$\varepsilon[P(h), \hat{W}(h), \hat{T}(h)] = 1 - \exp\left(\frac{-K(h)\ P(h)\ \hat{W}(h)}{\sqrt{\hat{T}(h)}}\right) \tag{12}$$

For the case of weak absorption

$$\varepsilon[P(h), \hat{W}(h), \hat{T}(h)] \simeq \frac{K(h)\ P(h)\ \hat{W}(h)}{\sqrt{\hat{T}(h)}} \tag{13}$$

where K incorporates the effective absorption coefficient, geometric and dimensional factors. Using a ratio formulation similar to that used for temperature, the constituent mixing ratio can be estimated from

$$\hat{W}_o\{P(z)\} = \hat{W}_c\{P(z)\}\ \frac{N_o(z)}{N_c(z)}\ \frac{B[\hat{T}_c(z)]\ P_c(z)\ \sqrt{\hat{T}_o(z)}}{B[\hat{T}_o(z)]\ P_o(z)\ \sqrt{\hat{T}_c(z)}} \tag{14}$$

This approximation works best when the selected climatological situation matches the observed radiances reasonably well and in regions of the atmosphere where the atmospheric opacity of the radiometric channel is not large. Also, the solution is reasonably stable in low signal to noise applications since errors made at high altitudes cannot propagate through the solution as is the case with onion peeling retrievals.

3.3.4 Iterative Inversions

As discussed by Gille (1972), the inversion of limb radiance observations is a non-linear problem. To efficiently employ a successive corrections approach, a fast technique for calculating radiance must be utilized. The concept of an emittance is carried one step further to accomplish this.

The limb radiance at tangent height h given by Eq. (1), and in Eq. (2) is approximated by a finite sum of contributions from discrete shells to be

$$I(h) \simeq \sum_{i=1}^{N} I'_i = \sum_{i=1}^{N} \bar{B}(T_i)\Delta\varepsilon(P_i, T_i, W_i). \tag{15}$$

Here $\Delta\varepsilon_i$ is the emissivity of the ith shell and $\bar{B}(T_i)$ is defined as

$$\bar{B}(T_i) = \sum_{j=1}^{M} B(\bar{\nu}_j\ T_i)\ \bar{R}_j\ d\nu \tag{16}$$

The shell emissivity is defined as

$$\Delta\varepsilon(P_I) = \frac{\sum_{j=1}^{M} B(\bar{\nu}_j, T_i)\ \bar{R}_j\ \Delta\tau(P_i, \bar{\nu}_j)}{\sum_{j=1}^{M} B(\bar{\nu}_j, T_i)\ \bar{R}_j} \tag{17}$$

and is calculated empirically using the forward radiance model.

In application, it is desirable to have the emissivity for all shells and tangent heights tabulated as a function of a single vertical coordinate to minimize the number of path integrals required for a radiance profile integration. Also, it is desirable to choose a parameterization that is relatively insensitive to the atmospheric state in

order to minimize the size of the climatological data set required to represent atmospheric variability. An empirical sensitivity study indicated that these requirements could be satisfied by writing

$$\tau = \exp\left(-k\sqrt{\overline{ap}}\right) \tag{18}$$

where $\overline{ap}$ is the vertical integral of the pressure weighted absorber amount a. The shell emissivity is then of the form

$$\Delta\varepsilon = -\Delta\tau = \frac{2k\,\tau\,\Delta\overline{ap}}{\sqrt{\overline{ap}}} \tag{19}$$

where $\Delta\overline{ap}$ is the contribution of the shell to the vertical integral of the pressure weighted absorber amount, and

$$\tau = 1 - \Sigma\Delta\varepsilon \tag{20}$$

where the summation extends over the shells along the ray path above the shell in question.

The variables of interest in the parameterization are then the effective absorption coefficients which implicitly contain all of the information about the geometry of a ray path through a given shell. For the jth shell and the ith tangent height, this parameter is then defined as

$$K_{ij} = 2k_{ij} = \frac{\Delta\varepsilon_{ij}\sqrt{(\overline{ap})_j}}{\tau_{ij}\,\Delta\overline{ap}_j} \tag{21}$$

The effective absorption coefficients for each shell are tabulated as a function of the vertical pressure weighted mass for all view angles. A family of such curves is shown in Figure 3.3.

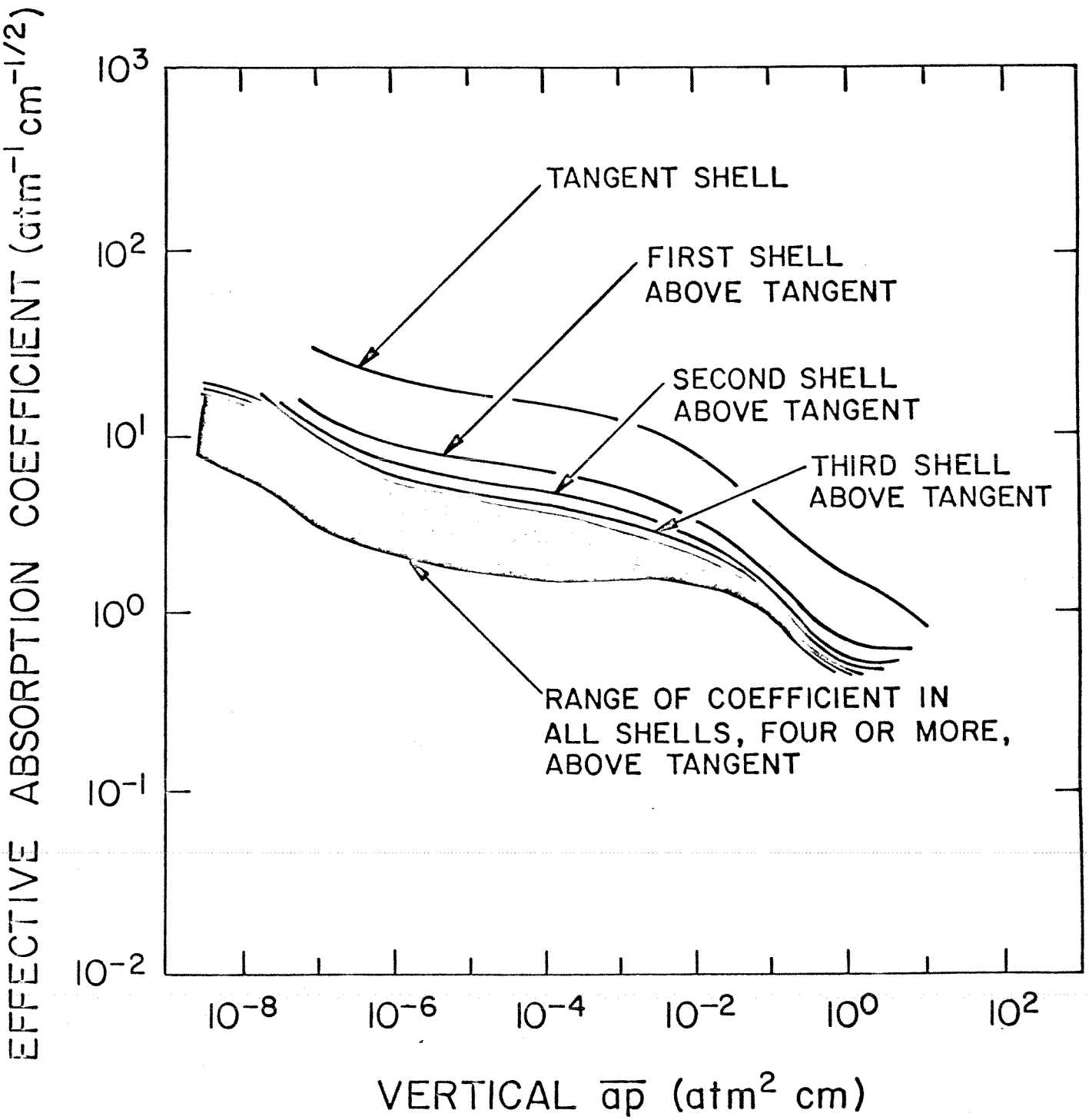

Figure 3.3 Family of effective shell absorption coefficients as a function of vertical pressure weighted mass.

To carry out a radiance calculation, the atmosphere is divided into a set of discrete shells. The emissivity for each shell is obtained by table look-up of the values shown in the curves and Eqs. (20 and 21). The contribution from each shell to the total radiance is then calculated using Eq. (15).

3.3.5 Temperature Inversion

Equation (15) provides the basis for the temperature inversion. The temperature dependence of the emissivity in each shell is assumed to be weak and the solution on the n-1 iteration reasonably close to that of the nth iteration. At the moment we will assume the pressure at each tangent height h is known. For these approximations, the following relationship may be written

$$I_{obs}(P(h_j)) - I_{cal}^{n-1}(P(h_j)) = \sum_{i=1}^{N} \Delta\varepsilon(P_i) \frac{\partial \bar{B}(T_i)}{\partial T_i} (T_i^n - T_i^{n-1}) \quad (22)$$

where the i=1 is the topmost shell in the atmosphere. The temperature adjustment in the shell corresponding to the first radiance point is calculated assuming all the radiance to originate from that shell. This correction is then distributed in the first scale height above and including the top shell. The upper boundary condition will be described in more detail below. Working down from the top, the temperature in each shell is adjusted by

$$T_N^n = T_N^{n-1} + \frac{[I_{jobs} - I_{jcal}^{n-1}] - \sum_{i=1}^{N-1} \Delta\varepsilon(P_i) \frac{\partial \bar{B}}{\partial T}(T_i^n - T_i^{n-1})}{\Delta\varepsilon_N \frac{\partial \bar{B}_N}{\partial T}} \quad . \quad (23)$$

Here N refers to the shell number corresponding to the observation and n to the iteration number. This procedure is carried out for both the wide CO_2 channel and the narrow CO_2 channel over the region of the atmosphere for which it is not saturated. In the region of overlap the final temperature solution for the nth iteration is a weighted average of the wide and narrow channel solutions given by

$$T_N^n = \frac{T^n_{\text{wide}_N} S_{\text{wide}} + T^n_{\text{narrow}_N} S_{\text{narrow}}}{S_{\text{wide}} + S_{\text{narrow}}} \qquad (24)$$

where S_{wide} and S_{narrow} are weights based upon the signal-to-noise ratios of the respective channels at each tangent pressure. In the part of the atmosphere where the narrow CO_2 channel is saturated, $S_{narrow} \rightarrow 0$ and the wide CO_2 channel solution is taken as the final solution. The differences between the wide and narrow channel solutions are then used to correct the pressure in the manner described in the next section. The process of temperature correction followed by pressure correction is iterated until the solutions converge.

The upper boundary condition is a potential source of error because no exact information on the temperature structure exists for altitudes above the top-most radiance measurement. In the case of LRIR, the temperature profile usually continues to decrease with altitude above this point. If an isothermal boundary condition is imposed, it is quite likely that the solution will be too cold at the altitude of the top-most radiance measurement. This error will propagate downward in the solution and take on alternating signs until it eventually damps out. In an effort to minimize this effect, an attempt was made to estimate the vertical gradient of the temperature profile at each iteration. The top of the atmospheric model was set at 4 scale heights above the top-most radiance measurement. The temperature in this boundary region varied linearly and joined the temperature solution at the fifth radiance sample from the top. The slope of the temperature in this region was determined by a least square fit using the top five temperature solution points and the upper boundary point of the atmospheric model from the previous iteration. A climatological value is used for the first iteration.

3.3.6 Pressure Profile Retrieval

The pressure inversion is performed in a manner similar to that described in Gille and House (1971). In the region between 10 and 25 mb, the optical characteristics of the wide and narrow CO_2 channels are reasonably different. For altitudes above 10 mb the outputs of the two channels become highly correlated. Around 15 mb the narrow CO_2 channel starts to become saturated while the wide CO_2 channel remains moderately transparent. The pressure retrieval is carried out by assigning a reference pressure P_o to a radiance sample point in the range 10-25 mb. Using this reference pressure and the temperature solution described in the previous section, the atmospheric pressure profile is built up using the hydrostatic equation. The difference between the wide and narrow channel temperature estimates is minimized using P_o as the adjustable parameter. The difference to be minimized is given by

$$\Delta T(P_o) = \sum_{i=m}^{n} [T_{wide_i} - T_{narrow_i}] \qquad (25)$$

where T_{wide_i} is the temperature solution from Eq. (29) at the ith pressure level using wide CO_2 channel radiances, and the reference pressure P_o. T_{narrow_i} is the corresponding solution using narrow CO_2 channel radiances. The shells m to n cover a range of pressures which were selected by sensitivity studies to provide the most unique information regarding P_o for the LRIR configuration.

The reference pressure on the last iteration P_o^{n-1} is updated by

$$p_o^n = p_o^{n-1} + \Delta T(p_o^{n-1}) \left[\frac{\partial \Delta T}{\partial p_o}\right]^{-1} \qquad (26)$$

where $\frac{\partial \Delta T}{\partial p_o}$ is computed by a finite perturbation of p_o. Using the new estimate of p_o, the pressure profile is again recalculated using the hydrostatic equation and the T^{n-1} distribution. The $\Delta\epsilon^n$ values for each shell and tangent path may then be computed and the nth iteration temperature inversion is performed.

3.3.7 Inversion for Constituent Mixing Ratio

Once the temperature and pressure at each point on the profile have been determined, the inversion for the ozone distribution can proceed. The difference between the observed and the calculated radiance for the jth tangent height at each iteration is given by

$$I_{obsj} - I^{n-1}_{cal_j} = \sum_{i=1}^{N} \bar{B}(T_i) \frac{\partial \varepsilon(P_i, W_i, T_i)}{\partial W_i} (W_i^n - W^{n-1}) \qquad (27)$$

The adjustment to the mixing ratios can be made in a manner similiar to temperature using differences in the observed and calculated radiances in an iterative manner.

$$W_N^n = W_N^{n-1} + \frac{[I_j^{obs} - I_j^{cal}] - \sum_{i=1}^{N-1} B_i \frac{\partial \varepsilon}{\partial w} (W_i^n - W_i^{n-1})}{\bar{B}[T_N] \frac{\partial \varepsilon(P_N),\ W_N^{n-1},\ T_N)}{\partial W}} \qquad (28)$$

This is a variation of the classical "onion peeling" method for retrieving constituent distributions from limb observations (e.g., Russell and Drayson, 1972). While this straightforward algorithm is relatively simple to implement, it becomes unstable for applications where the signal to noise ratio of the observations is not large. To constrain the solutions in regions of low signal to noise ratio, a variation of an approach suggested by Twomey (1977) was implemented. To avoid the problem of the solution going negative, a correction scheme involving a multiplier C(P(h)) that is a function of altitude is employed.

$$W_N^n = W_N^{n-1} * C_j \qquad (29)$$

Following Twomey (1977) such a corrector may be written in terms of the weighting functions as

$$C_j = [1 + (R_1 - 1)A_{1j}] [1 + (R_2 - 1)A_{2j}] \ldots [1 + (R_i - 1)A_{ij}] \quad (30)$$

where

R_i is the ratio of observed to calculated radiance at the ith level above tangent height j

A_{ij} is the normalized weighting function giving the contribution from level i to tangent height j

For the LRIR application, the radiance ratio is defined as

$$R_i = \frac{(N_{obs_i} + \sigma)}{(N_{cal_i} + \sigma)} \quad (31)$$

where σ is the instrument noise equivalent radiance for the channel in question. Adding this parameter has the effect of damping the amount of adjustment made to the initial solution profile as the signal to noise ratio approaches one. This process converges at about the same rate as the "onion peeling" formulation for weighting functions which pe the tangent point. When this property does not hold, such as in optically thick situations or when viewing tangent heights well below the maximum in the constituent concentration profile, the rate of convergence is less than that of Eq. (28). As a matter of economy, a combination of the two correction equations was used. The transition was made at a point where the rate of convergence of the multiplicative solution started to diminish and the signal to noise ratio was sufficient to obtain acceptable solutions via the onion peeling approach in the remaining lower part of the ozone profile.

Section 4

DATA QUALITY

4.1 Sounding the Stratosphere and Mesosphere by Infrared Limb Scanning from Space

Inversion of the measurements obtained by LRIR has demonstrated that quasi-global stratospheric and mesospheric temperatures and ozone concentrations may be obtained remotely from space with accuracy and precision comparable to in-situ methods.

Examples of typical temperatures and O_3 concentrations are shown by the solid lines in Figs. 4.1a and 4.2a, respectively. In-situ rocket comparison measurements are shown by the symbols. The altitude coverage is from 15 to 65 km, with vertical resolution adequate to resolve the 6 km temperature structure seen by the rocket ($\sim$ 50 km). There is good overall agreement between the temperature determination and the rocket measurement (Fig. 4.1a), and among all O_3 measurements except near the maximum, where the two rocket techniques show significant differences (Fig. 4.2a).

In order to assess the LRIR results, their accuracy and precision must be established. The precision, or repeatability, may be determined readily by calculating the standard deviation (σ) of a group of 12 to 16 sequential inversions, at a time and location for which atmospheric variations over the 300 to 400 km covered are minimal. The averages of several determinations are shown by dashed lines in Figs. 4.1b and 4.2b. These values result from an "end-to-end" evaluation, which includes the effects of atmospheric variations and data transmission, as well as instrument noise and data processing. For both temperature and O_3

concentration, the repeatability of the LRIR results is similar to (or perhaps slightly better than) that of rocket observations.

The accuracy of the LRIR results can be evaluated if one compares them with determinations made by another technique. As there is no absolute standard for stratospheric temperature determination, comparisons were made with in-situ measurements from the meteorological rocket network. The currently used Datasonde has been studied extensively; its accuracy is perhaps as good as 1 to 2 K over the altitude region of interest (15 to 65 km). Seventy-eight cases for which great circle distance between the rocket and the satellite overpass were $\leq 2°$ were used. The time differences were up to $\pm$ 12 hours for low- and mid-latitude summer and $\pm$ 3 hours otherwise. At each of 17 standard levels between 100 and 0.1 mb, the difference, LRIR retrieval minus rocket, was formed. The mean difference and standard deviation of the mean are also plotted in Fig. 4.1b.

With few exceptions, the differences between the LRIR and rocket results are not statistically significant and are within the Datasonde accuracy. Analysis by latitude shows no systematic trend in the differences. The determination of geostrophic winds depends upon horizontal gradients, which appear to be well preserved in the LRIR temperature retrievals.

Similarly, measurements made by rocket-borne optical and chemiluminescent instruments were used to assess the accuracy of the LRIR O_3 concentrations. The accuracies of both are difficult to determine but are estimated to be about 10 to 15 percent. The mean difference (rocket minus LRIR) of the four comparison cases and its standard deviation are presented in Fig. 4.2b. Above 30 km the differences are small, not

statistically significant, and within rocket instrument accuracy. Below 30 km the rocket values average 1 part per million by volume higher. Work is continuing in an effort to understand this difference.

Thus, for temperature and at least upper level O_3, and LRIR profile agrees with a coincident rocket measurement about as well as a second rocket would. The immediate conclusion is that infrared limb scanning, with available technology, provides results that are accurate and precise and that reproduce details of the vertical variation in the stratosphere and low mesosphere which cannot now be determined on a global basis in any other way.

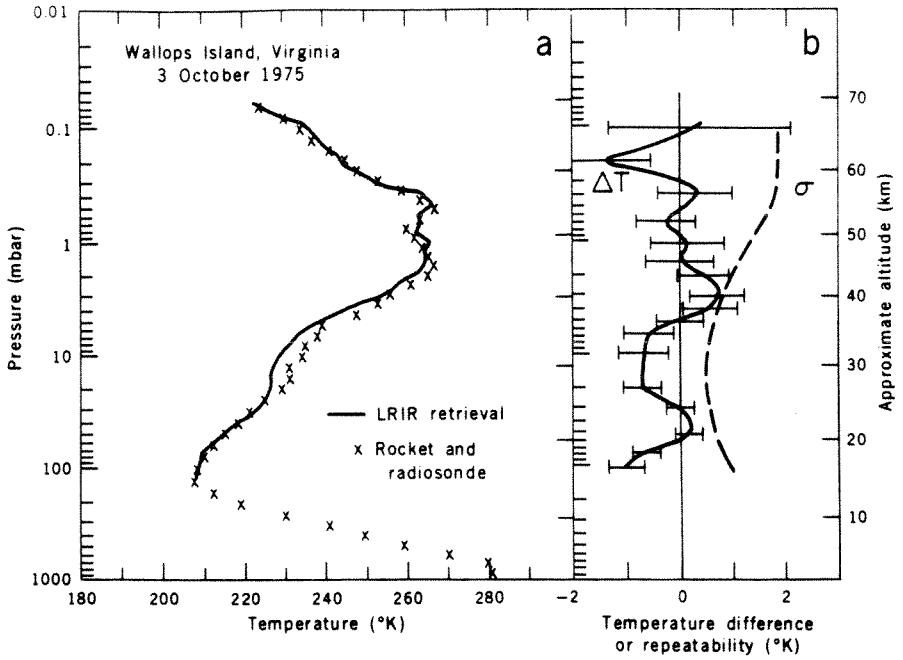

Fig. 4.1 Results of LRIR temperature retrievals. (a) Typical comparison of LRIR retrieval (solid line) and in-situ rocket and radiosonde measurements (symbols). (b) Statistical depiction of repeatability (1σ, dashed line) and accuracy, as evidenced by the mean difference (solid line) between 78 LRIR retrievals and near coincident in-situ measurements. Bars show the standard deviation of the mean differences.

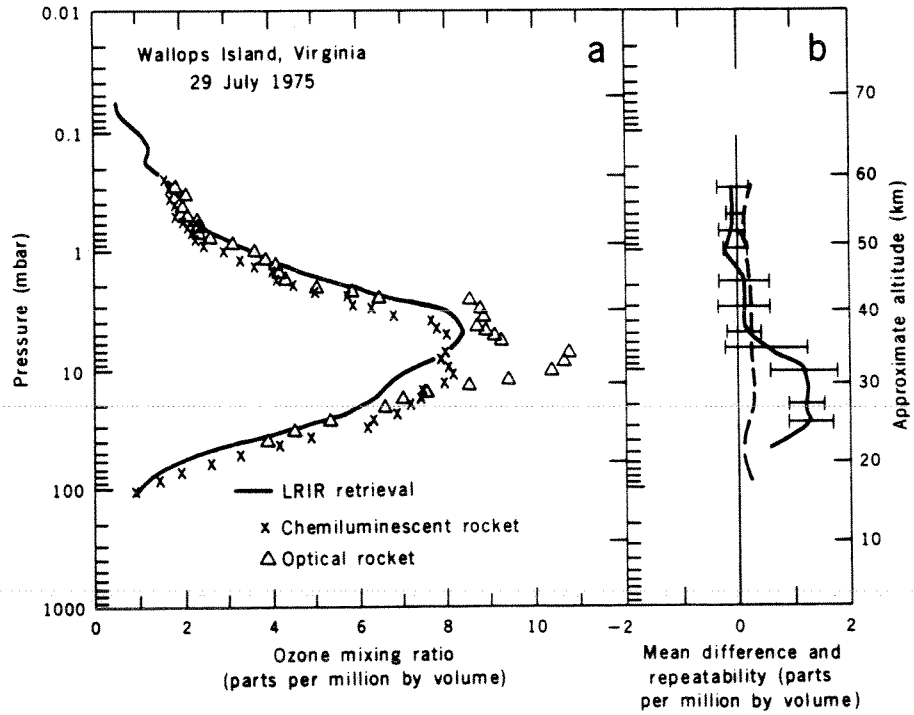

Fig. 4.2 Results of LRIR O_3 concentrations. (a) Typical comparison of LRIR retrieval (solid line) and in-situ rocket measurements (symbols). The mixing ratio is the number of O_3 molecules divided by the number of air molecules in a unit volume, in parts per million by volume. (b) Statistics of O_3 repeatability (1σ, dashed line) and accuracy, as evidenced by the mean differences (solid line) between four LRIR retrievals and near coincident in-situ measurements. Bars show the standard deviations of the mean differences.

Section 5

CATALOG AND SPECIAL EVENTS

Launch took place on June 12, 1975. The LRIR was first turned on at the beginning of orbit 35, on June 14, and began operating satisfactorily.

LRIR was operated at a 50% duty cycle until late October 1975. Thereafter, until January 7, 1976 it was operated at a 90% duty cycle. At that time the supply of methane in the solid cryogen cooler was completely expended and further collection of useful data ceased. The number of orbits which were recovered for each day of the mission are shown in Figure 5.1.

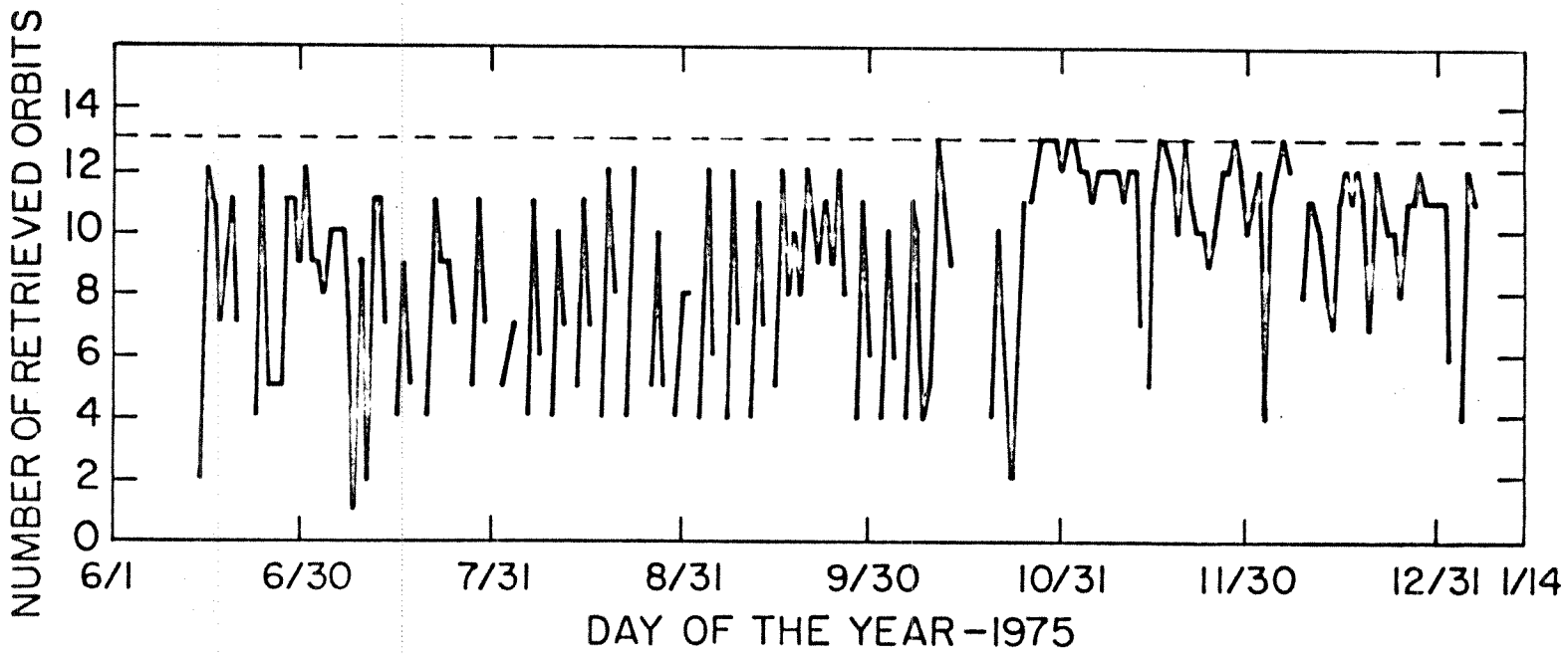

Figure 5.1 Number of orbits of data obtained for each day of the LRIR experiment.

Section 6

TAPE SPECIFICATION FOR LRIR

INVERTED PROFILE ARCHIVAL TAPE (IPAT)

The LRIR IPAT data are contained on 7 tapes. The tapes are 9 track, 1600 bpi with logical and physical record lengths of 17280 bits. See Figure 6.1 for the gross format. The following table briefly describes the contents of each tape.

Tape #	Dates	Orbits	Total # of Records	# of Files
1	6/20/75-7/30/75	105-648	13090	33
2	8/2/75-8/31/75	690-1078	7701	21
3	9/1/75-9/30/75	1085-1479	11163	25
4	10/2/75-10/31/75	1507-1899	10377	24
5	11/1/75-11/21/75	1901-2181	12887	21
6	11/22/75-12/14/75	2185-2489	11970	22
7	12/15/75-1/6/76	2492-2797	11316	22

Figure 6.1 Gross format

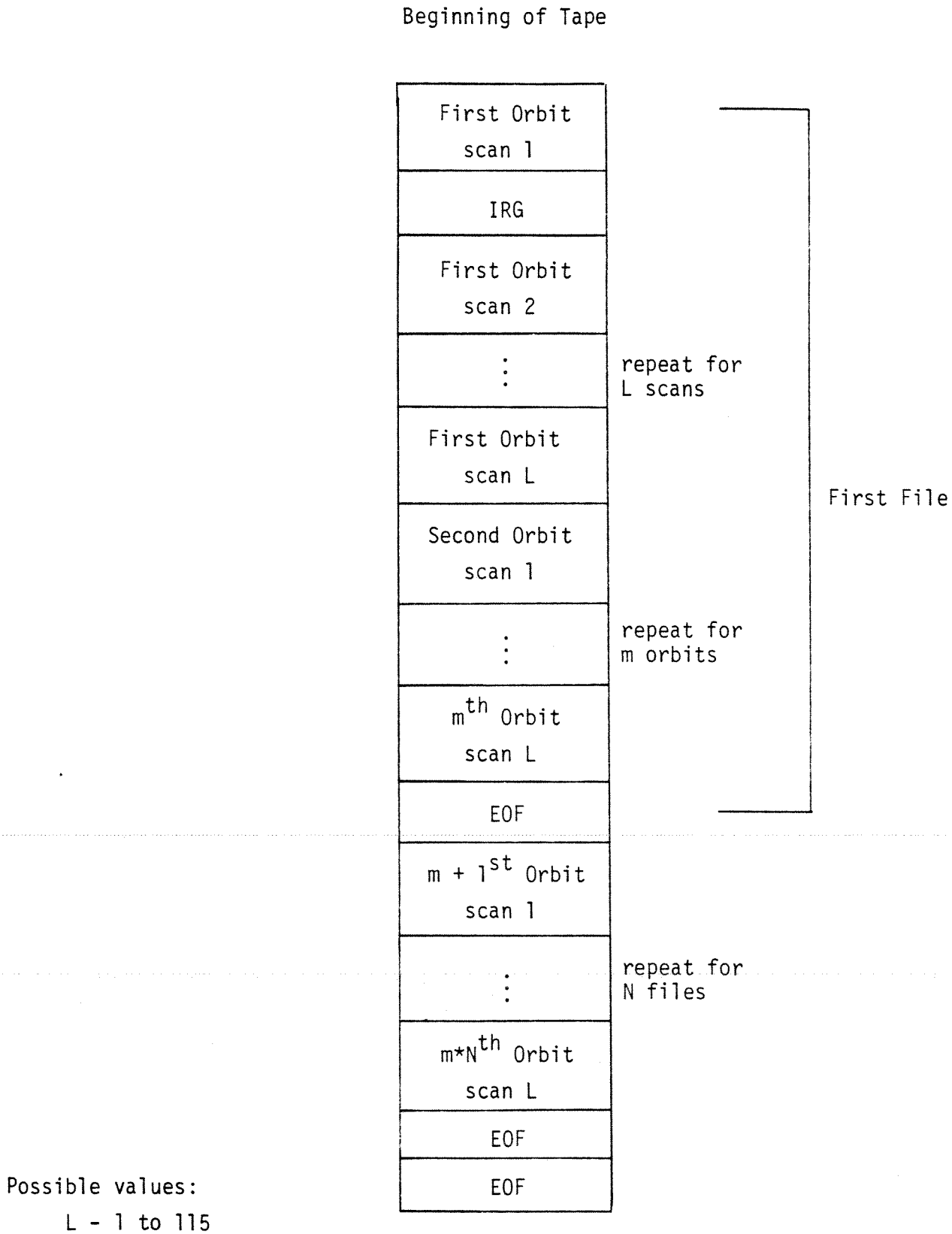

Possible values:

L - 1 to 115

m - 1 to 13 (approximately the number of orbits in a day)

N - 21 to 33

LRIR Inverted Profile Archival Tape (IPAT) Record

(1) Physical record number (32 bits)--This is the number of the record within a file. It starts at one and increments by one for each record in the file.

(2) File number (32 bits)--This is the number of the file on the tape. It starts at one and increments by one for each file on the tape.

(3) Orbit number (32 bits)

(4) Year (32 bits)

(5) GMT day (32 bits)

(6) GMT hour (32 bits)

(7) GMT minutes (32 bits)

(8) GMT seconds (32 bits)

(9) S/C altitude (32 bits)--Spacecraft altitude--To convert this value to a real floating point number, divide the value by 100.

(10) S/C latitude (32 bits)--Spacecraft latitude--To convert this value to a real floating point number, first subtract 9×10^5 from the value and then divide the result by 1×10^4.

(11) S/C longitude (32 bits)--Spacecraft longitude--To convert this value to a real floating point number, divide the value by 1×10^4.

(12) Tangent latitude (32 bits)--To convert this value to a real floating point number, first subtract 9×10^5 from the value and then divide the result by 1×10^4.

(13) Tangent longitude (32 bits)--To convert this value to a real floating point number, divide the value by 1×10^4.

(14) Number of pressure levels for this inverted profile set (32 bits).

(15) Number of radiance pressure levels for this profile set (32 bits).

(16) Pressure scale factor (32 bits)--This number is used for unpacking the pressure samples into units of mb. The unpacking procedure consists of dividing the pressure samples by the 32 bit integer scale factor and treating the result as a real floating point number.

(17) Temperature scale factor (32 bits)--This number is used for unpacking the temperature data into units of K. The procedure is the same as for the pressure scale factor (Item 16).

(18) Ozone scale factor (32 bits)--This number is used for unpacking the ozone mixing ratios into units of parts per million by volume. The procedure is the same as for the pressure scale factor (Item 16).

(19) Water vapor (H_2O) scale factor (32 bits)--This number will be used for unpacking the water vapor samples into units of parts per million. Currently, no water vapor mixing ratios are present.

(20) Narrow CO_2 radiance channel offset (32 bits)--This number is subtracted from the narrow CO_2 radiance sample before application of the scaling factor. This offset permits negative spikes to occur in the radiances for the purpose of allowing unbiased averages to be made.

(21) Wide CO_2 radiance channel offset (32 bits)--This number is subtracted from the wide CO_2 radiance sample before application of the scaling factor. This offset permits negative spikes to occur in the radiances for the purpose of allowing unbiased averages to be made.

(22) O_3 radiance channel offset (32 bits)--This number is subtracted from the O_3 radiance sample before application of the scaling factor. This offset permits negative spikes to occur in the radiances for the purpose of allowing unbiased averages to be made.

(23) Water vapor (H_2O) radiance channel offset (32 bits)--This number is subtracted from the H_2O radiance sample before application of the scaling factor. This offset permits negative spikes to occur in the radiances for the purpose of allowing unbiased averages to be made.

(24) Narrow CO_2 radiance channel scale factor (32 bits)--See item (39) for use.

(25) Wide CO_2 radiance channel scale factor (32 bits)--See item (40) for use.

(26) O_3 radiance channel scale factor (32 bits)--See item (41) for use.

(27) Water vapor (H_2O) radiance channel scale factor (32 bits)--See item (42) for use.

(28) Radiance-pressure offset index (32 bits)--This is the index in the radiance arrays that corresponds to the first pressure point.

(29) Index of cloud top (32 bits)--This is the index in all of the arrays that corresponds to the estimated cloud top or lowest altitude point in the retrievals.

(30) Cloud Top Pressure (32 bits)

(31) Stretch factor (32 bits)--This number divided by 1000 yields the multiplier applied to the nominal angular scale to correct for spacecraft motion.

(32) Twist factor (32 bits)--The distance the center of the wide CO_2 channel was offset from the center of the narrow CO_2 channel. To convert this number to a real floating point number with units of kilometers, first divide the number by 1000 and then subtract one.

(33) Ascending/Descending node flag (32 bits)--An ascending node flag is designated by the value of one. This corresponds to the data track moving south to north (and does not necessarily correspond to the movement of the satellite). A descending node flag (the data track moving north to south) is designated by the value of two.

(34) Algorithm ID (32 bits)--This is the version of the software used to modify the data. It is currently set to a value of one.

(35) Pressure Block (up to 45 levels of 32-bit words each)--To convert these values to real pressures with units of mb, divide the pressure value by the pressure scale factor. The array is designed to coincide with the radiance arrays and levels. Undetermined pressure values are zero filled.

(36) Temperature Block (up to 45 levels of 32 bit words each)--To convert these values to real temperatures with units of K, divide the temperature value by the temperature scale factor. The array is designed to coincide with the radiance arrays and levels. Undetermined temperature values are zero filled.

(37) Ozone mixing ratio block (up to 45 levels of 32 bit words each)--To convert these values to real mixing ratios with units of parts per million by volume, divide the mixing ratio value by the

ozone scale factor. The array is designed to coincide with the radiance arrays and levels. Undetermined ozone values are zero filled.

(38) Zero filled block (45 levels of 32-bit words each)--This section is reserved for possible addition of H_2O mixing ratio data at a future date.

(39) Narrow CO_2 channel radiance (up to 70 levels of 32-bit words each)--To convert these values to real radiances with units of $W\ m^{-2}\ sr^{-1}$, first subtract the narrow CO_2 radiance channel offset and then divide the result by the narrow CO_2 radiance channel scale factor. Undetermined narrow CO_2 values are zero filled.

(40) Wide CO_2 channel radiance (up to 70 levels of 32-bit words each)--To convert these values to real radiances with units of $W\ m^{-2}\ sr^{-1}$, first subtract the wide CO_2 radiance channel offset and then divide the result by the narrow CO_2 radiance channel scale factor. Undetermined wide CO_2 values are zero filled.

(41) Ozone channel radiance (up to 70 levels of 32-bit words each)--To convert these values to real radiances in units of $W\ m^{-2}\ sr^{-1}$, first subtract the ozone radiance channel offset and then divide the result by the ozone radiance channel scale factor. Undetermined ozone radiance values are zero filled.

(42) Water Vapor (H_2O) channel radiance (up to 70 levels of 32-bit words each)--To convert these values to real radiances in units of $W\ m^{-2}\ sr^{-1}$, first subtract the water vapor radiance channel

offset and then divide the result by the water vapor radiance channel scale factor. Undetermined water vapor radiance values are zero filled.

LRIR Archival IPAT Record

Word			Bits
1	Physical Record Number	(32)	32
2	File Number	(32)	64
3	Orbit Number	(32)	96
4	Year	(32)	128
5	Profile Time GMT Day	(32)	160
6	GMT Hour	(32)	192
7	GMT Minutes	(32)	224
8	GMT Seconds	(32)	256
9	S/C Altitude	(32)	288
10	S/C Latitude	(32)	320
11	S/C Longitude	(32)	352
12	Tangent Latitude	(32)	384
13	Tangent Longitude	(32)	416
14	Number of Levels for This Inverted Profile Set	(32)	448
15	Number of Radiance Levels for This Profile Set	(32)	480
16	Pressure Scale Factor	(32)	512
17	Temperature Scale Factor	(32)	544
18	Ozone Scale Factor	(32)	576
19	H_2O Scale Factor	(32)	608
20	NCO_2 Radiance Channel Offset	(32)	640
21	WCO_2 Radiance Channel Offset	(32)	672
22	O_3 Radiance Channel Offset	(32)	704
23	H_2O Radiance Channel Offset	(32)	736
24	NCO_2 Radiance Channel Scale Factor	(32)	768

25	WCO_2 Radiance Channel Scale Factor	(32)	800
26	O_3 Radiance Channel Scale Factor	(32)	832
27	H_2O Radiance Channel Scale Factor	(32)	864
28	Radiance-Pressure Offset Index	(32)	896
29	Index of Cloud Top	(32)	928
30	Cloud Top Pressure	(32)	960
31	Stretch Factor x 1000	(32)	992
32	(Twist Factor + 1) * 10000	(32)	1024
33	ASC/DESC Node Flag	(32)	1056
34	Algorithm ID	(32)	1088
35	First Pressure Level (Space Side)	(32)	1120
79	Second Pressure Level and Up to 45 Pressure Levels	(1408)	2528
80	Temperature at First Pressure Level	(32)	2560
124	Temperature at Second Pressure Level and Up to 45 Pressure Levels	(1408)	3968
125	O_3 Mixing Ratio at First Pressure Level	(32)	4000
169	O_3 Mixing Ratio at Second Pressure Level and Up to 45 Pressure Levels	(1408)	5408
170	H_2O Mixing Ratio at First Pressure Level (zero filled)	(32)	5440
214	H_2O Mixing Ratio at Second Pressure Level and Up to 45 Pressure Levels (zero filled)	(1408)	6848
215	NCO_2 Channel Radiance (Top Most Level)	(32)	6880
284	NCO_2 Channel Radiance at Up to 69 Additional Lower Altitudes Spaced 1.5 km	(2208)	9088
285	WCO_2 Channel Radiance (Top Most Level)	(32)	9120
354	WCO_2 Radiance at Up to 69 Additional Lower Altitudes	(2208)	11328
355	O_3 Channel Radiance (Top Most Level)	(32)	11360

424	O_3 Radiance at Up to 69 Additional Lower Altitudes	(2208)	13568
425	H_2O Channel Radiance (Top Most Level)	(32)	13600
494	H_2O Channel Radiance at Up to 69 Additional Lower Altitudes	(2208)	15808
	Spares	(1472)	
540			17280

540	32	Bit	Words
288	60	Bit	Words
270	64	Bit	Words

References

Bailey, P. L. and J. C. Gille, 1978: An approximate method for non-linear inversion of limb radiance observations. Remote Sensing of the Atmosphere: Inversion Methods and Applications, A. L. Fymat and V. E. Zuev, Eds., Elsevier Scientific Publishing Company, Amsterdam, pp. 115-122.

Bailey, P. L. and J. C. Gille, 1984: Inversion of limb radiance measurements. To be submitted.

Burn, J. W. and W. G. Uplinger, 1970: "The Determination of Atmospheric Temperature Profiles from Planetary Limb Radiance Profiles," NASA CR-1513.

Gille, J. C. and F. B. House, 1971: On the inversion of limb radiance measurements I: Temperature and thickness. J. Atmos. Sci., 28, 1427-1442.

Gille, J. C., 1972: Limb Radiance Inversion: Iterative Convergence for a Non-Linear Kernel," in Mathematics of Profile Inversion, L. Colin, Ed., NASA Tm X-62, 150.

Gille, J. C. and P. L. Bailey, 1977: Inversion of infrared limb emission measurements for temperature and trace gas concentrations. In Inversion Methods in Atmospheric Remote Sounding, A. Deepak, Ed., Academic Press, New York, pp. 195-216.

Gordley, L. L. and J. M. Russell III, 1981: Rapid inversion of limb radiance data using an emissivity growth approximation. Appl. Opt., 20, 807-813.

House, F. B. and G. Ohring, 1969: "Inference of Stratospheric Temperature and Moisture Variables from Observation of the Infrared Horizon," NASA CR-1419.

Rodgers, C. D., 1976: "Approximate Methods of Calculating Transmission by Bands of Spectral Lines." NCAR Technical Note. NCAR/TN-116+IA.

Russell, J. M. III, and S. R. Drayson, 1972: The inference of atmospheric ozone using satellite observations in the 1042 cm^{-1} band. J. Atmos. Sci., 29, 376-390.

Smith, W. L., 1969: "Polynomial Representation of Carbon Dioxide and Water Vapor Transmission," ESSA Technical Report NESC47.

Twomey, S., 1977: Introduction to the Mathematics of Inversion in Remote Sensing and Indirect Measurement. Elsevier Scientific Publishing Company, Amsterdam, pp. 243.

Appendices

A. Bibliography

B. Sounding the Stratosphere and Mesosphere by Infrared Limb Scanning from Space, by John C. Gille, Paul L. Bailey, Richard A. Craig, Frederick B. House, and Gail P. Anderson. From Science, Volume 208, pp. 397-399, 25 April 1980.

C. Temperature and Composition Measurements from the L.R.I.R. and L.I.M.S. Experiments on Nimbus 6 and 7, by J. C. Gille, P. L. Bailey and J. M. Russell III. From Philosophic Transactions of the Royal Society of London, Series A, Volume 296, pp. 205-218, 1980.

Bibliography

(Chronological)

Gille, J. C., 1968: On the possiblity of estimating diurnal temperature variation at the stratopause from horizon radiance measurements. J. Geophys. Res., 73, 1863-1868.

Gille, J. C., 1968: Inversion of radiometric measurements. Bull. Amer. Meteor. Soc., 49, 903-912.

Gille, J. C., and F. B. House, 1971: On the inversion of limb radiance measurements I: Temperature and thickness. J. Atmos. Sci., 28, 1427-1442.

Gille, J. C., 1972: Limb radiance inversion: Iterative convergence for a non-linear kernel. In The Mathematics of Profile Inversion, L. Colin, Ed., pp. 1-67 to 1-76, Washington, D. C., National Aeronautics and Space Administration, TM X-63150.

Gille, J. C., and P. L. Bailey, 1972: On the information content of limb radiance measurements. In Conference on Atmospheric Radiation Pre-print Volume, pp. 13-15, American Meteorological Society, Fort Collins, Colorado.

Bailey, P. L., and J. C. Gille, 1972: An improved algorithm for the inversion of limb radiance measurements. In Conference on Atmospheric Radiation Pre-print Volume, pp. 16-19, American Meteorological Society, Fort Collins, Colorado.

Gille, J. C., P. L. Bailey, F. B. House, R. A. Craig, and J. R. Thomas, 1975: The Limb Radiance Inversion Radiometer (LRIR) Experiment. In The Nimbus 6 User's Guide, J. E. Sissela, Ed., NASA Goddard Space Flight Center, Greenbelt, Md., pp. 141-161.

Gille, J. C., P. L. Bailey, R. A. Craig, F. B. House, 1977: Results from the Nimbus 6 Limb Radiance Inversion Radiometer (LRIR). In Proceedings of the Symposium on Radiation in the Atmosphere, H.-J. Bolle, Ed., pp. 305-308, Science Press, Princeton, N.J.

Bailey, P. L., and J. C. Gille, 1977: Precise calculations of limb emission for satellite application. In Proceedings of the Symposium on Radiation in the Atmosphere, H.-J. Bolle, Ed., pp. 301-304, Science Press, Princeton, N.J.

Gille, J. C., and P. L. Bailey, 1977: Inversion of infrared limb emission measurements for temperature and trace gas concentrations. In Inversion Methods in Atmospheric Remote Sounding, A. Deepak, Ed., pp. 195-216, Academic Press, New York.

Bailey, P. L., and J. C. Gille, 1978: An approximate method for non linear inversion of limb radiance observations. In Remote Sensing of the Atmosphere: Inversion Methods and Applications, A. L. Fymat and V. E. Zuev, Eds., pp. 115-122, Elsevier Scientific Publishing Company, Amsterdam.

Gille, J. C., and P. L. Bailey, 1978: Information content and results of non-linear inversion of Nimbus 6 Limb Radiance Inversion Radiometer data. In Remote Sensing of the Atmosphere: Inversion Methods and Applications, A. L. Fymat and V. E. Zuev, Eds., pp. 107-113, Elsevier Scientific Publishing Company, Amsterdam.

Gille, J. C., 1979: Middle atmosphere processes revealed by satellite observations. J. Atmos. Terr. Phys., 41, 707-722.

Gille, J. C., P. L. Bailey, and J. M. Russell III, 1980: Temperature and composition measurements from the LRIR and LIMS experiments on Nimbus 6 and 7. Phil. Trans. Roy. Soc. Lond. A, 296, 205-218.

Gille, J. C., P. L. Bailey, R. A. Craig, F. B. House, and G. P. Anderson, 1980: Sounding the stratosphere and mesosphere by infrared limb scanning from space. Science, 208, 397-399.

Gille, J. C., G. P. Anderson, and P. L. Bailey, 1980: Comparison of near coincident LRIR and OAO-3 measurements of equatorial night ozone profiles. Geophys. Res. Lett., 7, 525-528.

Gille, J. C., G. P. Anderson, W. J. Kohri, and P. L. Bailey, 1981: Observations of the interaction of ozone and dynamics. Proc. of Quadrennial International Ozone Symposium, Boulder, Colorado, 4-9 August 1980, pp. 1007-1011.

Anderson, G. P., J. C. Gille, P. L. Bailey, and S. Solomon, 1981: LRIR observations of diurnal ozone variations in the mesosphere. Proc. of Quadrennial International Ozone Symposium, Boulder, Colorado, 4-9 August 1980, pp. 580-585.

Kohri, W. J., 1981: LRIR observations of the structure and propagation of the stationary planetary waves in the Northern Hemisphere during 1975. NCAR Cooperative Ph.D. thesis. [NTIS PB82156639.]